Long Period (LP) Events on Mt. Etna volcano (Italy): the influence of velocity structures on moment tensor inversion

Claudio Trovato, I. Lokmer, Florent de Martin, Hideo Aochi

Geophysical Journal International Advance Access published July 30, 2016

Long Period (LP) Events on Mt. Etna volcano (Italy): the influence of Velocity Structures on Moment Tensor Inversion

Trovato C.[1],[2] *, Lokmer I.*[3] *, De Martin F.*[1] *, Aochi H.*[1][2]

[1]_ BRGM (Bureau de Recherches Géologiques et Minières), Orléans, France

[2]_ ISTO (Institut des sciences de la Terre d'Orléans), 1A bis, rue de la Férollerie, Orléans, France

[3]_ School of Earth Sciences, University College Dublin (UCD), Dublin, Ireland

Abstract

Since a few decades volcanic Long Period (LP) events have been recorded on many active volcanoes and their study has been recognized as an important tool to characterize volcanic activity. LP event analyses through moment tensor (MT) inversions have led to kinematic descriptions of various source mechanisms. The main challenge in these inversions is to "strip out" the propagation effect in order to isolate the source; hence the velocity model used controls the accuracy of the retrieved source mechanism. We first carry out several synthetic tests of inversions on Mt. Etna volcano (Italy). Four geological models with topography are considered with increasing complexity: the most complex model is used to generate synthetic data, while the other three models are used to calculate the Greens' functions for inversions. The retrieved solutions from the three velocity models are similar. The MT solutions for a deeper source are well retrieved, while a shallower source test suffers from high uncertainties and strong misinterpretation of the source orientation. The homogeneous model gives the lowest misfit value, but source location and mechanism decomposition are inaccurate. When a complex model different from the true one is used, a high misfit value and a wrong solution is obtained. We then incorporate our findings into the MT inversion of an LP event recorded on Mt Etna in 2008. We obtain very different solutions among the three models in terms of source location and mechanism decomposition. The overall shape of the retrieved source time functions are similar, but some amplitude differences arise, especially for the homogeneous

model. Our work highlights the importance of including the unconsolidated surface materials in the computation of Green's functions especially when dealing with shallow sources.

1. Introduction

The understanding of the origin of seismic signals on volcanoes is of fundamental importance to enhance our knowledge of volcanic systems and to monitor their activity. Volcanoes can exhibit a wide variety of seismic signal types (e.g. Chouet et al., 2006 and references therehein). Here we focus on long period (LP) seismic signals. LP events are characterized by low frequency waveforms (0.2 – 5 Hz) and are thought to have magmatic or hydrothermal origin (Chouet, 2003). They are often considered to be associated with resonance of fluid filled cavities (Aki et al., 1977; Chouet, 1996, 2003; Jousset et al., 2004; Nakano et al., 2003; Neuberg and Pointer, 2000) and their understanding is crucial to illustrate the shallow plumbing system of volcanoes. Recently, Bean et al., (2013) extended the observations of Harrington and Brodsky, (2007) and proposed an alternative model for explaining shallow LP seismicity. They analyzed the pulse-like nature of some LP events recorded on volcanoes and explained their origin as a slow failure of the weak shallow volcanic edifice close to the brittle-ductile transition. Their conclusions suggest that careful attention should be paid in using LP events as direct indicators of magmatic/hydortermal fluids.

An important tool to describe LP sources is moment tensor (MT) inversion (Davi et al., 2010; De Barros et al., 2011; Jousset et al., 2004, 2013; Kumagai et al., 2002, 2005; Lokmer et al., 2007; Nakano and Kumagai, 2005; Nakano et al., 2003). Many MT inversions on LP volcanic signals infer a tensile crack source mechanism (Eyre et al., 2013; Jousset et al., 2013; Kumagai et al., 2002, 2005; Nakano et al., 2003) . The orientations of these cracks span a full range from sub-horizontal to sub-vertical. A different source mechanism was obtained by Davi et al., (2010) on Arenal volcano (Costa Rica) where their analysis of a LP signal recorded for an explosion led to an isotropic source mechanism. Although the inversion process itself is well established, many questions on uncertainties arise due to the lack of

knowledge of the properties of materials traversed by seismic waves (Bean et al., 2008; Jousset et al., 2004). Although previously thought that kilometres long LP wavelengths are mostly insensitive to small variations of the volcanic structure, it has been shown that hundred meters thick superficial layers and features (volcanics above the sediments, dykes, magma pathways etc.) can significantly degrade source inversion efforts (Bean et al., 2008; Cesca et al., 2008; Kumagai et al., 2005; Neuberg and Pointer, 2000). This is because the complex stratigraphy of volcanoes has a strong impact on the seismic wavefield (Bean et al., 2008; Neuberg and Pointer, 2000). Nevertheless, many inversions were conducted in a homogeneous half-space (De Barros et al., 2011; Jousset et al., 2004; Kumagai et al., 2002; Legrand et al., 2000; Lokmer et al., 2007; Ohminato et al., 1998). There were also efforts to invert the source using a more complex media, such as a two-layered medium (Bean et al., 2008) or a heterogeneous medium (Davi et al., 2010; Eyre et al., 2015; Jousset et al., 2013); however, little is mentioned about the quantification of the introduced error in the case where the model is completely or partially incorrect. At present, detailed velocity structures of volcanoes are still rarely available (Davi et al., 2010). Here we extend the work of Bean et al., (2008) on the influence of the velocity structures on moment tensor inversion. We analyse the effect of different geological models with increasing complexities regarding their influence on successful source inversions.

We focus our attention on one of the most studied volcanoes in the world, Mt. Etna, located in eastern Sicily island (Italy), the largest active volcano in Europe. More than 600.000 people live nearby this active volcano (Chiarabba et al., 2000). It covers an area of about 1,250 km^2 and reaches a maximum elevation of ≈ 3.330 m. It's characterized by almost continuous eruptive activity from its summit craters and frequent lava flows from fissures opened on the flanks (Patanè et al., 2011). Due to the high volcanic activity many seismic signals are now recorded continuously (Saccorotti et al., 2007). Since 2003 the permanent network of

broadband stations has been installed by the INGV (Istituto Nazionale di Geofisica e di Vulcanologia) and LP events have been addressed in a number of strudies (Cannata et al., 2009, 2013; De Barros et al., 2009, 2011; Lokmer et al., 2007, 2008; Saccorotti et al., 2007). They appeared in periods of quiescence or during unrest episodes (Lokmer et al., 2007; Saccorotti et al., 2007). They are often difficult to be distinguished from the sustained volcanic tremor accompanying eruptions (Lokmer et al., 2008), but they may not be directly related to the eruption processes (De Barros et al., 2011; Saccorotti et al., 2007). The mechanism of the LP events suggested resonating phenomena at a relative shallow depth (~300-1200 m. below the summit) (De Barros et al., 2011; Lokmer et al., 2008). Recently, Bean et al., (2013) proposed a new model for explaining the shallow LP seismicity recorded in occasion of the 2008-2009 eruption of Mt. Etna (De Barros et al., 2009, 2011). They recognized that, while summit stations recorded pulse-like low-frequency signals, the same records on further stations appeared as classical resonating LP signals. They attributed the apparent resonance of these low-frequency seismic events to propagation effects and not being source related. Their model hypothesizes that those LP events are consequence of failure in materials close to the brittle-ductile transition. The brittle-ductile transition in shallow volcanic material is not supposed to be related to high temperature and pressure, but to the low friction angles of the unconsolidated shallow volcanic deposits. Similar conclusions have been drawn by Eyre et al., (2015) for Turrialba volcano, Costa Rica.

In this study we carry out a synthetic inversion verification test ("blind test"). We build four different structure models with increasing geological complexity. We suppose that the fourth most complex model corresponds to reality (state of reality) and that the three other models correspond to the best knowledge we have of the geological properties of the volcano (state of knowledge). Hence, we compute Green's functions for the first three models and synthetics data in the fourth most complex model for a tensile crack source mechanism. Thus, we will

perform three moment tensor inversions of this realistic synthetic dataset, using the Green's functions database outlined above. We vary the number of free parameters in our inversions, as well as the number of receivers. For the given synthetic scenario, we will discuss how well the inversion procedure can reproduce the original location, mechanism and source time functions using the different structure models and stations configuration. The use of synthetic scenarios allows us to extend the previous studies and to systematically assess the influence of the velocity model complexities to the accuracy of the retrieved source mechanism. We then extend the work of De Barros et al., (2011) analyzing a real LP event by means of the three geological models with variable complexity.

2. Models and Method

2.1 Velocity Models

Geological mappings of Mt. Etna volcano have been performed since more than a century. Surface units have been mapped by De Beaumont, (1836) and the first geological maps of Etna volcano were published in the 19th century (Waltershausen, 1844, 1880). In the last decades, official geological maps were updated twice (Branca et al., 2011; Romano et al., 1979) and many geological surveys have been carried out to map deposits along the steeps of Valle del Bove (Calvari et al., 1994; Coltelli et al., 1994) and integrate in the Italian geological map of the surroundings (Branca et al., 2009, 2011; Pasquare et al., 1992). On the other hand, many geophysical seismic surveys have been also carried out (Cardaci et al., 1993; Cauchie and Saccorotti, 2013; Chiarabba et al., 2000; Cristiano et al., 2010; Hirn et al., 1991; Laigle et al., 2000; Luca et al., 1997; Patane et al., 2002; Villaseñor et al., 1998) analyzing the velocity structure properties of the edifice. Following this studies we prepare four different models of the velocity structure by increasing its complexity on the depth

variation. All the models constructed with help of a meshing tool (CUBIT-13.2 from *Sandia Laboratories)* include topography from the Digital Elevation Model (DEM) of Mt. Etna with a 50 m spacing. Horizontally we prepare a model extending 19.6 km in the EW and 16 km in the NS direction, with a max height of about 3.300m (Fig. 1), large enough to minimize reflections from the model boundaries.

We use four (4) different models shown in Fig. 2. Model (S1) is homogeneous with P-wave velocity of 2000 m/s and Vp/Vs ratio of 1.73 (the value of 2000 m/s is taken from De Barros et al., (2009). The second model (*S2)* takes into account a low-velocity surface layer of 300 m thickness inferred from Bean et al., (2008). The third (*S3*) and the fourth (*S4*) models are more complex. In these two models we adopt the gradient model of Mt. Etna according to the geological map of Branca et al., (2011). The strong stratigraphic-gradient of the volcano is represented by different piled layers, thus are characterized by topography shape and become flatter with depth (towards a proportional smoothing function) until the sea level. We define the velocities at depth according to Branca et al., (2009), Chiarabba et al., (2000), Cristiano et al., (2010) and Patane et al., (2002). Model *S3* has a homogeneous surface layer of 300 m (Fig. 2). Model *S4* (Fig. 2) has a strong gradient structure in the shallow depths down to 360 m as inferred from Cauchie and Saccorotti, (2013). P-wave velocities (Vp) are derived from S-wave velocities (Vs) as, $Vp = \sqrt{3}Vs$ assuming a constant Poisson's ratio of 0.25. The material densities are computed following the formula proposed by Potter, (1998) in function of Vp. We use models *S1*, *S2* and *S3* to compute Green's functions for the inversion while model *S4* is used to compute the synthetic data.

Before interpreting the full waveforms computed in 3D complex geological media including sharp topography and non-planar layering, we look at the response of 1D layered structures consisting of horizontal layers overlying a homogeneous half-space with same profile as in Fig. 2. In addition to these geometric simplifications, the details of the seismic source are

avoided by considering a plane SH-wave propagating vertically from the half-space (i.e., no incidence angle has been considered). Under these hypotheses, only reflection/transmission of the SH-waves will occur at the interfaces; however, the interpretation of such simple configurations will give us valuable information about the impact of the 1D soil layering on vertically propagating SH-waves. For solving the 1D wave propagation in our four models S1 to S4, we compute the semi-analytical solutions in the frequency domain by the Thomson-Haskell propagator matrix method (Haskell, 1953; Thomson, 1950) and use the inverse Fourier transform to obtain the time domain waveforms. The plane wave is injected at 3km depth and the impulse source time function has a flat frequency spectrum up to 10 Hz. Fig. 3a shows the filtered (0.2 – 2 Hz) velocity waveform at the free surface. The waveform S1 has the exact shape of the source time function multiplied by a factor two. The original shape of the source time function is almost unchanged for models S3 while models S2 and S4 are significantly subjected to reflections/transmission effects due to the higher velocity contrast of the shallow layers. Model S3 shows arrival times comparable to the reference model S4, while those in models S1 and especially model S2 are considerably delayed (~1-1.5 s). Recorded amplitudes are higher for model S4 decreasing towards models S1. The frequency content of velocity traces (Fig 3b) shows a single peak for model S4 (f ~1.2 Hz) while the other models show different peaks with the main energy focused at lower frequencies. This simple comparison is obviously not representative of the complex Mt. Etna geological context with the presence of topography, but it clearly illustrates that models S1, S2 and S3 are different enough from model S4 to justify the proceeding of the synthetic test.

2.2 Methodology

In an elastic medium, the *n*-th component of the displacement (u_n) at a point *x* at a time *t* is given by the convolution between the source-time function of the moment/single force and the medium response, i.e. Green's functions (GFs) (modified from Aki and Richards, 2002):

$$u_n(x,t) = M_{pq}(t) * G_{np,q}(x,t) + F_p(t) * G_{np}(x,t) \qquad n,p,q = 1,2,3$$

Eq (1)

where M_{pq} is the *pq*-component of the seismic moment**,** F_p is the single force acting in the *p* direction and G_{np} represents the medium response (Green's function) for the *n*th-component displacement due to a unit single force F_p and $G_{np,q}$ means the spatial derivative with respect to the *q*-component at the source position. The asterisks indicate an operation of convolution and the Einstein summation convention is applied.

The numerical method used to compute the synthetic seismograms is the spectral-element method (SEM). This method has been developed in computational fluid dynamics by Patera and Maday (Maday and Patera, 1989; Patera, 1984). It was then introduced in computational seismology a decade later to compute with accuracy wave propagation in complex geological media (Faccioli et al., 1997; Komatitsch and Vilotte, 1998). The SEM is a high-order finite-element approximation in which the consistent choice of an orthogonal polynomial basis and of a Gauss numerical quadrature leads to the convergence properties of spectral methods. Because of the use of high-order piecewise polynomials basis, numerical dispersion is significantly reduced compared with the classical finite-element method (FEM) (De Basabe and Sen, 2007; Seriani and Oliveira, 2008). The reader is referred to Komatitsch et al., (2005) and Chaljub et al., (2007) for review articles presenting the numerous developments of SEM, and to Moczo et al., (2014) for a historical presentation and recent applications to seismic wave propagation in alluvial valleys.

The FEM, and therefore the SEM, is particularly well adapted to compute wave propagation in media where the relief features (such as mountains, hills, creeks or volcanoes) are present because the free surface condition (and more generally the continuity of traction) is said to be a "natural boundary condition". In other words, the free surface, no matter what shape it has, is accounted for in the weak form of the equations to be solved and does not have to be explicitly enforced at the elemental level. This allows surface topography to be accounted for in SEM, as long as the elements can honor the shape of the free surface without any aliasing. For this study, a special care has been taken for the generation of the meshes so that the finite elements of size 50 m at the free surface follow the volcano's topography provided by a digital elevation model (DEM) of resolution 25 m.

In this article, to calculate GFs in the elastic medium with irregular surface topography and synthetic seismograms, we use the open-source code EFISPEC3D (http://efispec.free.fr). This computer program (under double licenses CeCILL-V2 and GNU-GPL-V3) solves the three-dimensional equations of motion using a continuous Galerkin spectral-element method. The correctness of the implementation of the spectral-element method into this code has been thoroughly verified in De Martin, (2011) and Chaljub et al.,(2015). EFISPEC3D is used in computational seismology to better understand the impact of lithological and topographic effects on near-surface Green's functions (Maufroy et al., 2015).

We put potential source positions within a volume of 1.000 x 1.000 x 800 m^3 located below the main crater of Etna volcano between 2.2 km a.s.l. and 3 km a.s.l. (Fig. 1). Among the 28 receivers used in this study, 13 receiver locations correspond to the stations of the permanent network operated by INGV, 12 are from temporary surveys (De Barros et al., 2009; Lokmer et al., 2007; Saccorotti et al., 2004) and 3 receivers (synthetic stations) are added to guarantee the azimuthal coverage for our synthetic test (Fig. 1). In order to treat a large number of

source locations we take advantage of the reciprocity (Aki and Richards, 2002) to calculate GFs.

We carry out the inversion in frequency domain for eq. (1), which is schematically written as a vector-matrix equation:

$$\mathbf{u} = \mathbf{Gm}$$

Eq (2)

where **u** is the data matrix, **G** contains the Green's functions and **m** is the moment tensor and single forces components that we aim to obtain. We perform the inversion for the model parameters **m** without applying any a priori constraints to the solution (hereafter called "unconstrained inversion"). We define the misfit (R) function as:

$$R = \frac{(\mathbf{u} - \mathbf{Gm})^T(\mathbf{u} - \mathbf{Gm})}{\mathbf{u}^T\mathbf{u}}$$

Eq (3)

where superscript *T* denotes a transposed matrix. The least-squares solution of eq. (2) is given by (e.g., Menke, 1989):

$$m^{est} = (\mathbf{G}^T\mathbf{G})^{-1}\mathbf{G}^T\mathbf{u}$$

Eq (4)

This inverse problem (eq. 2) can be solved either for six independent moment tensor components (MT) (assuming no single forces), or six moment tensor plus three single forces (MT+F). The inversion is carried out for each position of the source (14196 positions at 40 m

spacing). Comparing the value of the misfit R from each inversion we can estimate the best fitting source position. For analyzing the estimated solution in terms of their mechanism, we use the principal component analysis (PCA) through a singular value decomposition (SVD) (Cesca and Dahm, 2008; Vasco, 1989). This technique assumes the existence of a unique source time function (STF) for all the six components of the moment tensor (see Vasco, 1989 for further details). We then decompose the moment tensor solution into isotropic (M_{ISO}) and deviatoric (M_{CLVD} + M_{DC}) parts after Jost and Herrmann, (1989) and Vavryčuk, (2001).

Additionally, we also perform a constrained inversion following the approach by Lokmer et al., (2007), assuming either a tensile crack or isotropic source mechanism. Eq. (2) is rewritten as

$$u = GM_0 f(\phi, \theta)$$

Eq. (5)

where $\boldsymbol{f}$ is a function of strike ϕmeasured from the North in the clockwise direction and dip θ, independent of frequency. Our inversion reduces to finding a single parameter $M_0(\omega)$. We perform the grid search spanning from 0° to 360° for strike (ϕ) and from 0° to 90° for dip (θ), every 10° for the tensile crack mechanism. For an isotropic source one inversion is enough as the function $\boldsymbol{f}$ has a unique expression.

The inversion procedure has been verified for different source mechanisms by producing synthetic data in the velocity model S2 and inverting with Green's function for the same velocity model. MT inversion and SVD delivered the perfect solution validating our implementation.

2.3 Synthetics data

Previous inversions of LP signals on Etna volcano (De Barros et al., 2011; Lokmer et al., 2007) suggest quasi-vertical crack orientations. Hence we simulate, as the synthetic source mechanism, a point source of a vertical tensile crack (ϕ=45°, θ=90°) at two different depths located below the summit craters: at 2.880 m.a.s.l. (shallow source, ~400 m depth) and at 2.240 m.a.s.l (deep source, ~1.2 km depth). We use a Ricker wavelet as source time function with the main energy in the frequency range 0.2 – 1.2 Hz (typical for LP events, Chouet, 2003) and an amplitude of 4 x 10^{10} Nm. As already mentioned, model S4 is used to calculate the data. Time step is Δt = 1 x 10^{-4} s, for a duration t_{tot} = 20 s. A single simulation of 2.3 x10^{6} hexahedron elements takes about 18 hours on 192 cores on our local server (AMD Abu Dhabi at 1.6 GHz). Synthetic data are computed without adding noise.

So, for each velocity model we calculate three inversions, MT (moments only), MT+F (moments plus single forces) and CONSTR (constrained inversion).

3. Results

We first carry out the unconstrained inversion in order to investigate the reliability of the solution and the uncertainty between the different velocity models.

In the following, we will discuss the source location, the source mechanism and the source time function obtained from MT/MT+F inversions with models *S1, S2* and *S3*. The 12 stations located nearby the summit, offering a proper azimuthal coverage, are used (Appendix A and Appendix B). We choose to include only 12 stations located in the near-intermediate field, as we want to mimic realistic number of available stations.

3.1 Source location

First, for the two given source depths (~400 m and ~1.2 km depth), we explore how well the inversion procedure can retrieve the true position in different structural models. We evaluate the misfit from the moment tensor plus single force (MT+F) inversions. The comparisons of the best fit waveforms for the shallow and deep sources are shown in Appendix A and Appendix B, respectively. The overall shape of the original signals is well reproduced in all three velocity models. The stations closer to the source reproduce better the original source time function (STF) shape as, for small distances, the wavefield is less subjected to attenuation, scattering and reflection phenomena. This is the case for stations *et08*, *et06* and *et09*, while differences on the waveforms are stronger for farther stations (e.g. *cl01* and *et99*).

Fig. 4 shows the misfit *R* computed iteratively for each point in the 3D grid for the MT inversion at all the possible source locations in each velocity model and the misfits are summarized in Tables 1 and 2. For the shallow source, the minimal misfit found in model *S2* coincides with the original source position. For models *S1* and *S3* the obtained source locations are shallower (~100 m) than the original one, at the upper limit of our parameter search. The synthetic test has been built as a "blind test", and a further computation of Green's functions is computationally expensive. Hence, we consider these locations as a local minima and not a global one.

For the deep source we get good (~200 m distance from the original position) horizontal and vertical resolution for both *S1* and *S2* models. For model *S2* the location is slightly better constrained, as the lowest misfit value sharply converges to a single position. For model *S1* we can observe a large spreading of low misfit values, even if the lowest misfit still points to the right source position. The reason is that the shape of the waveform in a homogeneous model is very weakly affected by the perturbations of the deep source location around its true position. Model *S3* points to a quite distant (~400 m from the original position) source location and the value of misfit (Table 1) is considerably higher than the two other models.

Epicentral locations both for the shallow and deep sources are very well constrained except for the deep source in the velocity model *S3*. The good radial/azimuthally station coverage guarantees a good resolution in retrieving the original epicentral position. The non-negligible influence of the strong velocity gradient in the shallow part of model *S4* is better resolved when considering simple velocity models *S1* and *S2*. On the opposite, especially for the deeper source, the velocity contrast reproduced in model *S3* degrades the solution. This implies that a simple model is better to use if we do not know exactly the velocity structure. This is particularly evident for the deeper source where lateral heterogeneities play a major role (Appendix B). On the other hand, vertical locations are less resolved and appear more sensitive to the wrong velocities definition.

In summary, source location towards MT-Inversion (and especially vertical resolution) is very sensitive to the choice of the velocity model. The results obtained here, even for such a simple case (there is no noise and the reference model *S4* is still simple if compared to reality) point out that other locations methods such as amplitude decay, cross-correlation coefficient and semblance (Cannata et al., 2013 and references therein) less sensitive to velocity definition should instead be used.

3.2 Source mechanism

For the best source position obtained above, the source orientation and isotropic/deviatoric decomposition for each model are estimated in Table 1(shallow source) and Table 2 (deep source). We compute as well the moment magnitude of the selected event as:

$$M_w = \frac{(\log(M_0) - 9.1)}{1.5}$$

Eq. (6)

where M_0 is the highest absolute retrieved seismic moment after SVD.

3.2.1 Shallow source

The crack strike (ϕ) is well retrieved for both inversions (MT+F and MT) while the obtained crack dip (θ) is close to a solution of a horizontal crack rather than a vertical one for the solution including single forces. The minimum misfit *R* is found for model *S1*. In terms of isotropic/deviatoric decomposition, the MT+F inversion points to the right ratio, letting the predominant component in C_{ISO}, C_{DC} being close to zero and C_{CLVD} showing values close to the given one for all three models. The MT inversion without single forces points to a very low C_{CLVD} value and a high C_{DC}. In this case the mechanism would be interpreted differently with a strong double-couple component and a mixed ISO/DC solution.

3.2.2 Deep source

Table 2 shows the results for the deep vertical crack. Again the lowest misfit values are found for *S1* model (both MT+F and MT solutions). Model *S3* shows a very high misfit value. The crack strike (ϕ) and dip (θ) angles are very similar to the true ones for all the three models and the best solutions are obtained for model *S1* (MT+F) and *S2* (MT+F). In terms of mechanism, the decompositions for models *S1* and *S2* give a low C_{DC} component and the crack solution is well retrieved, while model *S3* tends to overestimate the C_{DC} component (16% for the MT+F solution). The same observations are brought for the MT inversion except that we find higher C_{DC} component contributions.

In summary, we find that model *S1* gives the lowest misfit value in both the MT+F and MT inversions for both source depths. The crack orientation is better retrieved by model *S2* such as the isotropic/deviatoric decomposition. For the shallow source it is difficult to retrieve the right crack dip angle with any of the velocity models in the MT+F solutions; the shallow vertical crack might be interpreted as a shallowly dipping one. The dip angles are better retrieved when considering MT solutions, but we are still far from the right orientation angle.

Moreover, when not considering single forces, we find very high C_{DC} values which complicate the interpretation of the solution. The magnitude of the event is quite well retrieved by all solutions (Table 1): slightly overestimated for MT+F (especially model *S1*) and slightly underestimated for MT-only (except model *S1*). The strong retrieved single forces have the effect to increase the strength of the seismic moment. This is probably due to interference of the radiated seismic waves by both the MT and single forces On the opposite, the deep source orientation is well retrieved by all the three velocity models for both solutions MT+F and MT-only. The retrieved values for the magnitude of the event (Table 2) are equivalent between MT+F and MT-only solutions (slightly underestimated in respect to the expected event magnitude) and the appearance of spurious single forces does not influence the energy of the radiated seismic waves. In first approximation, the "blind test" tells us that little matters the chosen velocity model, we encounter problems in defining the right source orientation for shallow sources, but for deep ones things turn out to be better and we always obtain a good solution. The inability in retrieving the correct solution for the shallow source could be due to the strong velocity contrast just below the ground surface of velocity model *S4*. The shallow crack source is embedded inside these low velocity sector, hence none of the three Green's functions models is able to model correctly the strong impedance contrast of model *S4* (especially near-field terms, Lokmer and Bean, 2010) and this eventually leads to errors which tend to be accommodated by single forces which, in turn, degrade the MT solution. The same does not apply for the deeper source because of the longer paths followed by waves and predominance of intermediate- and far-field effects.

In order to explore the influence of the strong velocity contrast of model *S4* on the retrieved MT components for each velocity model, in the next section we compare our retrieved source time functions for each MT component with the expected ones.

3.3 Source time function

Figs. 5 and 6 show the comparison between the original source time function (STF) and the retrieved one for MT+F and MT inversions respectively. For a better comparison we define the validation misfit as

$$V = \sum_{n=1}^{N} \frac{(\mathbf{MT_R} - \mathbf{MT_T})^T (\mathbf{MT_R} - \mathbf{MT_T})}{(\mathbf{MT_T})^T \mathbf{MT_T}}$$

Eq (7)

where $\mathbf{MT_R}$ is the retrieved MT solution, $\mathbf{MT_T}$ is the original MT tensor and N is the number of time series.

3.3.1 MT+F

In the MT+F inversion the force terms show high amplitudes especially for model *S1* (Fig. 5) and different orientations spanning from sub-horizontal to sub-vertical directed NE to SW not coherent with the orientation of the original tensile crack source mechanism. This is consistent with De Barros et al., (2013) who showed that spurious single forces were generated to accommodate converted waves at layered interfaces. A force with an amplitude of 10^8 N s generates comparable seismic excitation to a seismic moment of 10^{11} Nm (Aki and Richards, 2002; De Barros et al., 2013), i.e. leading to waves of the same order of amplitude (if the radiation pattern is neglected or averaged across the network). For the shallow source inversions, the validation misfits (Table 1 and Table 2) between the original and the retrieved source time functions (considering only the MT terms) are very high for the three models. Model *S1* shows the highest validation misfit (28.972). Model *S2* shows the best match with the original solution. The original STF is generally well reproduced (especially models *S2* and *S3*), but the M_{zz} component suffers of overestimation in amplitude thus leading to the high

validation misfit and the wrong source mechanism orientation interpretation. For the deep source, the amplitudes of the seismic moment are always underestimated. The validation misfits are considerably lower than for the shallow source with model *S1* showing better correspondence with the original source time function. Anyway, the overall shape of the retrieved STF is similar and well reproduced for all different models.

3.3.2 MT-only

The MT inversion (Fig. 6) shows similar results, but the validation misfits are considerably lower than the solution including forces and the original source time functions are better reproduced. Again, the *Mzz* component of the shallow source does not match the true solution especially for the simplest model *S1*. This is due to the *quasi*-horizontal layering in which the wave conversions occur. Models *S2* and *S3* show comparable validation misfits (~0.85) and the amplitudes of the moment tensor components are comparable to the original STFs.

For the deep source the misfit values are lower, the same as for the MT+F solution. Best matching between the original and the retrieved solution is obtained by model *S1* (validation misfit = 0.545). The overall amplitude of the STF is in general underestimated, likely because the velocity at depth is much lower in *S1* than in the true model *S4*.

In summary, the synthetic test shows that the deep source mechanism is correctly retrieved by both the MT+F and MT solutions. The shallow source, on the other hand, suffers from large errors in the retrieved STF which strongly influence the mechanism decomposition (as highlighted previously in Cesca et al., 2008). Main uncertainties for the shallow source are due to the large leakage between the true and retrieved M_{zz} component. This implies that we are unable to correctly resolve the isotropic component of the MT. Consequently, the MT+F solutions and the MT solution for model *S1* would be interpreted as a shallowly dipping tensile crack. The MT solution for models *S2* and *S3* point to a quasi-vertical crack as

expected, but the appearance of the non-existing double-couple components complicates the mechanism interpretation.

3.4 Constrained Inversion

Finally we perform the constrained inversions. Our input source is a vertical tensile crack oriented 45° clockwise from North. We perform the inversion assuming a tensile crack and an isotropic source, respectively. The results are summarized in Table 3 and the Misfit results for the crack mechanism are shown in Appendix C and Appendix D. All models show a good solution with the lowest misfit indicating a tensile crack mechanism and pointing to the correct angles (strike (ϕ) and dip (θ)) orientation for both the shallow and the deep source in the given parameter ranges. Figs. 7 and 8 show the comparison between the original and retrieved STFs for all three models and depths from the inversions with and without single forces, respectively. The retrieved amplitudes in models *S1* are overestimated in all the inversions. The amplitude is twice than expected for the shallow source. STF shape is well retrieved in both models *S2* and *S3* for the solutions with and without singles forces. For the deep source a phase shift between the original and retrieved STF occurs due to travel time delays caused by different velocity model. Generally both models *S2* and *S3* offer a good solution in both angle pairs and STF, while model *S1* tends to overestimate the STF amplitude.

We now apply our results obtained by the synthetic test to the inversion of a real event recorded at Mt Etna.

4. Real Case: an LP event in 2008

Despite our synthetic test has been designed to mimic reality, in the real world MT inversion is subject to significant uncertainties which should strongly influence our ability in retrieving the correct solution. Here we want to show the influence of the choice of a particular velocity model on the inversion process, thus we carry out an inversion of an LP event recorded on Etna in 2008 during a high resolution seismic survey (De Barros et al., 2009, 2011). The considered event was recorded on June 19, 2008 and belonged to the second family of events identified in De Barros et al. (2009). The source mechanism was analyzed (De Barros et al., 2009, 2011) a) by locating the event with a time delay technique based on cross correlation and b) by identifying the source mechanism performing a MT inversion using a homogeneous model (same as our model *S1)*. The mechanism was retrieved as a sub-vertical crack oriented ϕ=N340° E and inclined θ=50° (see De Barros et al., (2011) for further details). While De Barros et al., (2011) used 16 stations in their inversion, we choose 12 stations with a good azimuthal distribution around the source (Appendix E) in order to reproduce a context similar to the one chosen for our synthetic test.

4.1 Unconstrained inversion

Appendix E shows the comparison between the original filtered data and our synthetics resulting from the MT+F inversion for the three models separately. Stations *etsm* and *et08* show the highest amplitude signal and thus contribute more to the final solution. For these two stations we get a good correspondence between the observed and the retrieved signals for all three models. Farther stations do not reproduce the increased complexity in the observations, for example at stations *emfs* and *emcn.* For the MT+F inversion, the location solution (Fig. 9) for model *S2* shows the lowest misfit value and is also closer to the location

determined by De Barros et al. (2011); however, our location is shifted horizontally by about 450 m and vertically by 200 m, quite far from the source location found by De Barros et al. (2011). Models *S1* and *S3* suggest even deeper locations with lerger horizontal differences (≈ 650 m). We then apply PCA on the obtained solutions in each inversion. Similar to De Barros et al., (2011), we obtain a high M_{ISO} component in both MT+F and MT inversions (Table 4). Model *S2* for the MT+F solution shows the lowest M_{ISO} value (79 %) and a relatively high M_{DEV} (21%) component. Like De Barros et al., (2011), we perform a MT decomposition (according to Vasco, 1989) on the M_{DEV} part of our MT+F and MT inversion solutions. For model *S2*, MT+F solution, the results show a strike of ϕ=90° and a dip of θ=21°, i.e. a sub-horizontal crack instead of the sub-vertical obtained by De Barros et al., (2011). The MT+F solution from models *S1* and *S3* also varies, in particular in terms of strike. The dip of θ=67° from model *S3* is comparable to the one found by De Barros et al., (2011). Fig. 10 shows the retrieved STF for the three models after the MT inversion. Here the MT solution in model *S1* shows a higher amplitude than the two other models. As MT and MT+F solutions are often used to estimate the volume of fluids or gas mobilized at the source (Davi et al., 2010; Hidayat et al., 2002; Jousset et al., 2013; Ohminato et al., 1998), it is obvious that the results may be very uncertain, depending on the discrepancy of the used velocity model from the true one. The amplitude difference is also present in MT+F case but it is less remarkable. The overall shapes of the retrieved STFs for the three models are quite similar and model *S2* shows the simplest solution. For all the three models, the diagonal of the moment tensor is largely dominant while non-diagonal elements show much lower amplitude. Non-diagonal elements in the solution without single forces tend to be overestimated compared to the solution including forces.

4.2 Constrained inversion

The high C_{ISO} components retrieved for the unconstrained inversion for the three velocity models suggest a possible isotropic source mechanism and so does the constrained inversion which shows slightly lower misfit values for the explosion solution (MT+F, Table 5). It is worth noticing that a tensile crack with a low Poisson's ratio in the source region could also lead to the same eigenvalues ratio. In terms of the orientation of the crack solution, the parameter search for the MT+F solution does not indicate a clear orientation (Appendix F). The MT+F solution shows a narrow range of misfit values spanning from 0.44 to 0.5 for models *S1* and *S2*, and from 0.5 to 0.6 for model *S3*. The minimum misfit found for model *S2*, MT+F solution, shows a strike orientation similar to the one found by De Barros et al., (2011), but the inclination of the fault once again results in a sub-horizontal instead of a sub-vertical crack. The MT-only solution results more stable, and all three models point to the same solution ($\phi = \approx 300°$ and $\theta = \approx 50°$), but the misfit values are very high (≈ 0.8). As the misfit values for the constrained inversion fall in a very narrow range, the solution is subject to difficult interpretations, i.e. it is difficult to discriminate between an isotropic and a tensile crack source mechanism.

5. Quantifying the "goodness of solution"

In this section, we quantify the reliability and sensitivity of the solution in our inversion framework. In order to achieve this task, the Green's functions should be repeatedly calculated for a large number of perturbed velocity models. However, in 3D heterogeneous medium with topography this would be extremely computationally expensive, hence we use a different approach instead: for each velocity model, we perform a large number of inversions for randomly chosen network configurations. In this way we implicitly include different parts

of velocity models into inversions. From such a large number of solution for a particular velocity model we calculate (i) robustness of the inversion for a given model, and (ii) departure of the retrieved from the true model. In this test, all MT inversions are performed for the fixed source location at the original point in order to get rid of errors due to mislocation and tackle directly the influence of the velocity model on the source mechanism.

We select 21 seismic stations located at distances shorter than 5 km from the source. We then randomly select 8 to 16 stations from the available 21. In this way we obtain 1350 station combinations and, for each of them, we perform MT-inversion for all the three velocity models and both source depths. After applying PCA to the MT solutions we analyze the source properties and orientation as outlined in section (2.2). For each velocity model/source combination, we compute the median and the absolute median deviation. In order to make the results more intuitively comprehensible, we also compute the slip direction α after Vavryčuk, (2001) representing the angle between the fault plane and the slip vector, i.e. $\alpha = 90°$ for a pure tensile mechanism, while $\alpha = 0°$ for a pure shear faulting.

The results of MT+F and MT-only inversions for both the sources are reported in Fig. 11. The results confirm many of the conclusions outlined during the previous synthetic test (section 3). Model S1 always delivers the lowest misfit in both MT+F and MT-only inversions, but for the shallow source it also leads to the worst validation misfit in both the MT+F and MT-only inversions.

More generally, we find that the MT+F inversion (Fig. 11a and Fig. 11c) is always able to retrieve the correct strike (ϕ) for both the shallow and deep sources, but it fail to correctly determine the dip (θ) ($\theta \approx 45°$) for the shallow source and well retrieves it for the deeper one. Finally the angle α is well retrieved for the shallow source, but is highly underestimated for the deeper one ($\alpha \approx 50°$), i.e. the mechanism would be misinterpreted as a mixed tensile/shear source.

When we focus on the MT-only solutions (Fig. 11b and Fig. 11d), both the strike and dip orientations are well retrieved for both the sources even if the dip angle for the shallow source is affected by high uncertainties. We also find that the angle α is underestimated for both the sources and the results show again high uncertainties (especially for the shallow source). The C_{DC} component is very high ($C_{DC} \approx 40\%$) for both the sources.

In the following paragraph we compare the validation misfits (expressed as L1-norm departure between the retrieved and the true solution) for each MT component. (Fig. 12a). Looking at the MT+F solutions (Fig. 12a), the shallow source shows the high validation misfits for all the components. The worst result is obtained in M_{zz} component, especially for velocity models S1 and S2, and this leads to the wrong dip angle retrieved after MT decomposition. Model S3 shows lower validation misfits in all the MT components for the shallow source, but the MT decomposition still points to the wrong source orientation. The deep source shows lower validation misfits and the three models deliver comparable (and acceptable) results. Compared to the MT+F solutions, the validation misfits from the MT-only inversion (Fig. 12a) are considerably lower for both the shallow and the deep sources. In addition, the MT-only solution is less sensitive to the selected subset of stations (smaller fluctuations around the median solution). In this case the worst result is obtained again for the M_{zz} component from model S1; also, the off-diagonal components show quite a large departure from their true values for the shallow source. Generally, including single forces in the solution degrades the match between the observed and the retrieved STFs. M_{zz} is the most affected component and simple models (S1 and S2) deliver the worst results.

On the other hand, in order to figure out the stability of the inversion process, we plot (Fig. 12b) the validations misfit against the number of the receivers used in the MT inversion. The validation misfit tends to decrease when increasing the number of stations. This is particularly evident for the shallow source (both the MT+F and MT-only solutions) and for the

homogeneous model S1 (The validation misfit is double when using 8 instead of 16 stations). However, we do not see any significant improvement in the retrieved source parameters (not showed here). The convergence of the results does not mean that we get the original source mechanism more closely by simply playing on the stations network. For the shallow source, including 16 stations (realistic case for real LP events) in the MT inversion is not enough to obtain acceptable results. In all the synthetic tests, we always misinterpret one of the source parameters, either dip or α angles. More generally, none of the velocity models leads to the correct solution (shallow source), while the three velocity models deliver very similar results.

6. Discussion

6.1 Implications of the results

We performed synthetic tests to investigate the sensitivity of seismic source inversion results to the choice of the structural model. The homogeneous model (*S1)* shows lower misfit values than the other complex velocity models, but the retrieved STFs strongly deviate from the original ones, especially for the shallow source. On the other hand, the model with the highest degree of complexity (*S3*), which should better represent the complexity of model *S4*, does not give any better results. The reason is a large departure of the shallow portion of the model *S3* from the model *S4* (see Fig. 2). Finally model *S2* offers the best result in our synthetic test. It is worth nothing that the lowest misfit values obtained for the shallow source with model *S1* correspond to the highest validation misfit values computed between the observed and retrieved STFs, leading to an important conclusion that the smallest inversion misfit does not always corresponds to the most accurate source mechanism (the same conclusion as in Bean et al., 2008). In the synthetic tests the results are similar and an approximately good solution

can always be retrieved for each considered velocity model (i.e. the shallow source mechanism is well retrieved when a constrained inversion is performed; for the deep source we get a good solution even for an unconstrained inversion). Then we analyzed a real event recorded on Mt Etna during a high resolution seismic campaign in 2008. Our results show that, in this particular case, the model with the lowest misfit value is the surface layer model *S2*. The analysis of a real LP event highlights the influence of the choice of a particular velocity model on the retrieved solution, i.e. the interpretation of the source mechanism varies for each considered velocity setting. These differences in convergence of the solutions between the synthetic and real data sets could arise because in the synthetic tests we are dealing with a simplified version of the reality. In particular, we ignored the following facts: any noise in the signal, complex source process different from a simple tensile vertical crack and further heterogeneities in the velocity model (especially lateral heterogeneities). All these factors are common for most MT inversions of LP events performed everywhere and could be source of errors in the retrieved MT solutions.

6.2 General remarks

The inversion tests were performed using the topography of the Etna volcano, but the overall remarks can be taken into account in any MT inversion for real LP events at volcanoes. The summary of our observations is given below:

1. Location: Locating events by the MT inversion grid search may lead to an incorrect source location and its mechanism (see results for model S3 in section 3). Thus, we suggest to locate the events with some alternative technique, less sensitive to the choice of velocity model.

2. Inclusion of single forces: De Barros et al., (2013) suggest that the inclusion of single forces into MT inversions accommodates errors arising due to the mismodelling of the structural properties of the volcanic edifice. This is demonstrated by showing the equivalence of the radiation pattern of the vertical force in a homogeneous medium and that of the converted S-waves at the low-velocity interface inside volcanic edifice. However, their examples apply for a flat medium without topography. Our results here show that although the inclusion of single forces can indeed accommodate the mismodelling in certain cases, it generally increases the discrepancy of the retrieved from the true solution. In addition, there is a significant energy leakage between the vertical force and the Mzz component, so we suggest to generally avoid the MT+F inversions.

3. Shallow source: The solutions for the shallow source are strongly influenced by the generation of the surface waves and converted phases present in the waveforms calculated for model *S4*, hence the inversion is subjected to high uncertainty and misinterpretation. Adding complexities in the velocity model used to compute Green's functions does not necessarily lead to the correct solution. Generally better results are obtained without single forces, but this leads to spurious double-couple components. Even without the inclusion of single forces, the Mzz component for shallow sources shows increased sensitivity to the shallow part of velocity models.

4. Deep source: Deep source is well retrieved by all the models for not constrained and constrained inversions.

5. Constrained inversion: Good results for the orientation of the shallow crack can be obtained for every velocity model only when performing a constrained inversion (same conclusion as in Bean et al., 2008 and Lokmer et al., 2007). On the other hand, when dealing with real data the constrained inversion may deliver ambiguous results. If a converged solution cannot be found when performing a constrained inversion, we should move to different strategies (inversion of tilt components (Chouet and Dawson, 2015; van Driel et al., 2015; Maeda et al., 2011; Thun et al., 2015), lower frequencies etc.)

6. Velocity model: An important question addressed in this study is whether including complexities in the velocity model improves our ability in retrieving the original source mechanism. The synthetic tests show that, for the deep source, the three velocity models deliver similar and acceptable results. However, the model S1, with the underestimated velocity at depth, overestimates the STF. It suggests that in the case of deep sources, the best available tomographic model should be used. One the other hand, for shallow sources, the vertical component (M_{zz}) of the MT tends to be incorrectly retrieved by any velocity model. A likely reason for this is improperly captured surface waves and pronounced converted phases present in the wavefield. This makes the results for shallow sources unreliable and directly affects our efforts to estimate the amount of gas/magma involved in the source processes. To summarize, for deep sources we are allowed to use a simple velocity model of the volcano (if a comprehensive description of the geological properties is not available), but for shallow sources one should be aware of the issues outlined above. In such cases the inversion should be carefully performed with more constraints (constrained inversions

if there is any clue about the nature of the source, or possibly the inclusion of tilt) or in much lower frequency band, less sensitive to structural heterogeneities.

7. Lowest misfit: The lowest misfit values are not synonym for the best solution. The lowest residuals obtained for the shallow source for model *S1* shows the highest discrepancy between the original and retrieved STFs. This is an important remark and caution should be exercised when interpreting results.

8. Double-couple components: Moderately high, spurious double-couple components arise in all model interpretations and are particularly evident in the MT-only solutions. This should be carefully investigated by synthetic tests when trying to interpret real events showing non-negligible shear components.

The summary of our synthetic tests outlined above suggests that the unconstrained inversions for shallow sources with approximate velocity models cannot guarantee correct source solutions. However, it is important to mention that this strong conclusion is obtained from testing inversions in a standard LP frequency band (0.2- 2 Hz). It is likely that much better results could be obtained by shifting the scope toward much longer periods and including into inversions both translational ground motion and tilt.

7. Conclusion

We investigated the sensitivity of the moment-tensor inversion solution to the choice of velocity models under a volcanic context. Four models with increasing geological complexity have been used in our synthetic test. Since both the source location and inversion are jointly

affected by the uncertainties in the velocity model, we suggest that, when possible, LP events should be first located by other location methods (such as amplitude decay, cross-correlation coefficient and semblance e.g. Cannata et al., 2013 and references therein), and then inverted for the best source position. In this way, computational resources for calculating many Green's functions could be attributed for testing various velocity models. If it is not possible to carry out the extensive synthetic testing and there are clues about the nature of the source mechanism, we suggest performing a constrained MT inversion in order to find out the most plausible source mechanism. This is in agreement with the suggestions given in Lokmer et al. (2007) and Bean et al. (2008). Solutions obtained for a shallow source and a homogenous model (*S1*) tend to overestimate the real amplitude of the source time function (in both constrained and unconstrained inversions), hence caution should be exercised when estimating the gas/fluid volumes (possibly) involved in the generation of LP events. Under the presence of shallow unconsolidated volcanic materials, especially when considering shallow sources, all the tested velocity models delivered high uncertainties in the results. In particular, the solution including forces (MT+F) led to an incorrect source mechanism, so we suggest to avoid this type of inversions. Although the results obtained by MT-only inversion exhibit significantly less fluctuation and smaller departure from the true mechanism, they often include a large amount of spurious shear component. Based on the outlined observations, we propose to use the MT-only inversion for deep sources, while the constrained inversion (possibly combined with MT-only) should be used for shallow sources.

It is important to remind that our tests are performed in a typical LP frequency band (0.2 – 2 Hz), so our conclusions are applicable to this frequency band only. A recent research presented the case where there exists energy in the very-low frequency band ($f < 0.1$ Hz) of some LP events (Thun et al., 2015). In such a cases, the strategy may be extending the band of inversion towards the low frequencies, which are less sensitive to the structural

heterogeneities. Also, apart from the translational signals, the tilt could be included into inversions (e.g. van Driel et al., 2015 and Maeda et al., 2011). Such a joint translational/rotational very-low frequency inversions appear to be a necessary step towards improving our ability to reliably determine a source mechanism from recorded data, and it will be the subject of future work

Further works on the understanding of the material properties of volcanoes and their response to waves with wider frequency content would strongly improve our understanding of the physical mechanism beyond LP events generation.

Acknowledgments

The research leading to these results has received funding from the People Programme (Marie Curie Actions) of the European Union's Seventh Framework Programme (FP/72007-2013) under the project NEMOH, REA grant agreement 289976. We are grateful to L. De Barros for providing us the Etna data. We also thank to F. Boulahya for supporting our numerical simulations and G. Saccorotti and L. De Barros for taking part in the discussion of addressing uncertainties. The comments from the two anonymous reviewers were helpful to improve the manuscript.

References

Aki, K., Fehler, M., and Das, S. (1977). Source mechanism of volcanic tremor: fluid-driven crack models and their application to the 1963 kilauea eruption. J. Volcanol. Geotherm. Res. *2*, 259–287.

Aki and Richards (2002). Quantitative Seismology, Second Edition. (University Science Books.).

Bean, C., Lokmer, I., and O'Brien, G. (2008). Influence of near-surface volcanic structure on long-period seismic signals and on moment tensor inversions: Simulated examples from Mount Etna. J. Geophys. Res. Solid Earth *113*.

Bean, C.J., De Barros, L., Lokmer, I., Métaxian, J.-P., O' Brien, G., and Murphy, S. (2013). Long-period seismicity in the shallow volcanic edifice formed from slow-rupture earthquakes. Nat. Geosci. *7*, 71–75.

Branca, F., S., Coltelli, M., Groppelli, G., and Pasquarè, G. (2009). Note illustrative alla carta geologica d'Italia alla scala 1:50.000. Foglio 625 Acireale.

Branca, S., Coltelli, M., Groppelli, G., and Lentini, F. (2011). Geological map of Etna volcano, 1:50,000 scale. Ital. J. Geosci. *130*, 265–291.

Calvari, S., Groppelli, G., and Pasquarè, G. (1994). Preliminary geological data on the south-western wall of the Valle del Bove, Mt Etna, Sicily. Acta Volcanol. *5*, 15–30.

Cannata, A., Montalto, P., Privitera, E., Russo, G., and Gresta, S. (2009). Tracking eruptive phenomena by infrasound: May 13, 2008 eruption at Mt. Etna. Geophys. Res. Lett. *36*.

Cannata, A., Di Grazia, G., Aliotta, M., Cassisi, C., Montalto, P., and Patanè, D. (2013). Monitoring Seismo-volcanic and Infrasonic Signals at Volcanoes: Mt. Etna Case Study. Pure Appl. Geophys. *170*, 1751–1771.

Cardaci, C., Coviello, M., Lombardo, G., Patané, G., and Scarpa, R. (1993). Seismic tomography of Etna volcano. J. Volcanol. Geotherm. Res. *56*, 357–368.

Cauchie, L., and Saccorotti, G. (2013). Probabilistic inversion of Rayleigh-wave dispersion data: an application to Mt. Etna, Italy. J. Seismol. *17*, 335–346.

Cesca, S., and Dahm, T. (2008). A frequency domain inversion code to retrieve time-dependent parameters of very long period volcanic sources. Comput. Geosci. *34*, 235–246.

Cesca, S., Battaglia, J., Dahm, T., Tessmer, E., Heimann, S., and Okubo, P. (2008). Effects of topography and crustal heterogeneity on the source estimation of LP events at Kilauea volcano. Geophys J Int *172*, 1219–1236.

Chaljub, E., Komatitsch, D., Vilotte, J.-P., Capdeville, Y., Valette, B., and Festa, G. (2007). Spectral-element analysis in seismology. Adv. Geophys. *48*, 365–419.

Chaljub, E., Maufroy, E., Moczo, P., Kristek, J., Hollender, F., Bard, P.-Y., Priolo, E., Klin, P., De Martin, F., Zhang, Z., et al. (2015). 3-D numerical simulations of earthquake ground motion in sedimentary basins: testing accuracy through stringent models. Geophys. J. Int. *201*, 90–111.

Chiarabba, C., Amato, A., Boschi, E., and Barberi, F. (2000). Recent seismicity and tomographic modeling of the Mount Etna plumbing system. J. Geophys. Res. Solid Earth *105*, 10923–10938.

Chouet, B. (1996). New methods and future trends in seismological volcano monitoring (Monitoring and mitigation of volcanic hazards Scarpa/Tilling (eds). Springer-Verlag Berlin Hieldelberg).

Chouet, B. (2003). Volcano seismology. Pure Appl. Geophys. *160*, 739–788.

Chouet, B., and Dawson, P. (2015). Seismic source dynamics of gas-piston activity at Kīlauea Volcano, Hawaii. J. Geophys. Res. Solid Earth *120*, 2525–2560.

Chouet, B., Dawson, P., and Nakano, M. (2006). Dynamics of diffusive bubble growth and pressure recovery in a bubbly rhyolitic melt embedded in an elastic solid. J. Geophys. Res. *111*.

Coltelli, M., Garduno, V.H., Pompilio, M., Neri, M., and Pasquare, G. (1994). Geology of the northern wall of Valle del Bove, Mt Etna (Sicily). Acta Vulc *5*, 55–68.

Cristiano, L., Petrosino, S., Saccorotti, G., Ohrnberger, M., and Scarpa, R. (2010). Shear-wave velocity structure at Mt. Etna from inversion of Rayleigh-wave dispersion patterns (2 s < T < 20 s). Ann. Geophys. *53*.

Davi, R., O'Brien, G.S., Lokmer, I., Bean, C.J., Lesage, P., and Mora, M.M. (2010). Moment tensor inversion of explosive long period events recorded on Arenal volcano, Costa Rica, constrained by synthetic tests. J. Volcanol. Geotherm. Res. *194*, 189–200.

De Barros, L., Bean, C.J., Lokmer, I., Saccorotti, G., Zuccarello, L., O'Brien, G.S., Métaxian, J.-P., and Patanè, D. (2009). Source geometry from exceptionally high resolution long period event observations at Mt Etna during the 2008 eruption. Geophys. Res. Lett. *36*, n/a – n/a.

De Barros, L., Lokmer, I., Bean, C.J., O'Brien, G.S., Saccorotti, G., Métaxian, J.-P., Zuccarello, L., and Patanè, D. (2011). Source mechanism of long-period events recorded by a high-density seismic network during the 2008 eruption on Mount Etna. J. Geophys. Res. *116*.

De Barros, L., Lokmer, I., and Bean, C.J. (2013). Origin of spurious single forces in the source mechanism of volcanic seismicity. J. Volcanol. Geotherm. Res. *262*, 1–6.

De Basabe, J., and Sen, M. (2007). Grid dispersion and stability criteria of some common finite-element methods for acoustic and elastic wave equations. GEOPHYSICS *72*, T81–T95.

De Beaumont, E. (1836). Recherche sur la structure et l'origine du Mount Etna. *ser. 3, 9*.

De Martin, F. (2011). Verification of a Spectral-Element Method Code for the Southern California Earthquake Center LOH.3 Viscoelastic Case. Bull. Seismol. Soc. Am. *101*, 2855–2865.

van Driel, M., Wassermann, J., Pelties, C., Schiemenz, A., and Igel, H. (2015). Tilt effects on moment tensor inversion in the near field of active volcanoes. Geophys. J. Int. *202*, 1711–1721.

Eyre, T.S., Bean, C.J., De Barros, L., O'Brien, G.S., Martini, F., Lokmer, I., Mora, M.M., Pacheco, J.F., and Soto, G.J. (2013). Moment tensor inversion for the source location and mechanism of long period (LP) seismic events from 2009 at Turrialba volcano, Costa Rica. J. Volcanol. Geotherm. Res. *258*, 215–223.

Eyre, T.S., Bean, C.J., De Barros, L., Martini, F., Lokmer, I., Mora, M.M., Pacheco, J.F., and Soto, G.J. (2015). A brittle failure model for long-period seismic events recorded at Turrialba Volcano, Costa Rica. J. Geophys. Res. Solid Earth *120*, 1452–1472.

Faccioli, E., Maggio, F., Paolucci, R., and Quarteroni, A. (1997). 2d and 3D elastic wave propagation by a pseudo-spectral domain decomposition method. J. Seismol. *1*, 237–251.

Harrington, R.M., and Brodsky, E.E. (2007). Volcanic hybrid earthquakes that are brittle-failure events. Geophys. Res. Lett. *34*.

Haskell, N.A. (1953). The dispersion of surface waves on multilayered media. Bull. Seismol. Soc. Am. *43*, 17–34.

Hidayat, D., Chouet, B., Voight, B., Dawson, P., and Ratdomopurbo, A. (2002). Source mechanism of very-long-period signals accompanying dome growth activity at Merapi volcano, Indonesia. Geophys. Res. Lett. *29*, 33–1 – 33–34.

Hirn, A., Nercessian, A., Sapin, M., Ferrucci, F., and Wittlinger, G. (1991). Seismic heterogeneity of Mt Etna: structure and activity. Geophys. J. Int. *105*, 139–153.

Jost, M.L., and Herrmann, R.B. (1989). A Student's Guide to and Review of Moment Tensors. Seismol. Res. Lett. *60*, 37–57.

Jousset, P., Neuberg, J., and Jolly, A. (2004). Modelling low-frequency volcanic earthquakes in a viscoelastic medium with topography. Geophys. J. Int. *159*, 776–802.

Jousset, P., Budi-Santoso, A., Jolly, A.D., Boichu, M., Surono, Dwiyono, S., Sumarti, S., Hidayati, S., and Thierry, P. (2013). Signs of magma ascent in {LP} and {VLP} seismic events and link to degassing: An example from the 2010 explosive eruption at Merapi volcano, Indonesia. J. Volcanol. Geotherm. Res. *261*, 171–192.

Komatitsch, D., and Vilotte, J.-P. (1998). The spectral element method: An efficient tool to simulate the seismic response of 2D and 3D geological structures. Bull. Seismol. Soc. Am. *88*, 368–392.

Komatitsch, D., Tsuboi, S., Tromp, J., and others (2005). The spectral-element method in seismology. Geophys. Monogr.-Am. Geophys. UNION *157*, 205.

Kumagai, H., Chouet, B.A., and Nakano, M. (2002). Waveform inversion of oscillatory signatures in long-period events beneath volcanoes. J. Geophys. Res. Solid Earth *107*, ESE 7–1 – ESE 7–13.

Kumagai, H., Chouet, B.A., and Dawson, P.B. (2005). Source process of a long-period event at Kilauea volcano, Hawaii. Geophys. J. Int. *161*, 243–254.

Laigle, M., Hirn, A., Sapin, M., Lépine, J.-C., Diaz, J., Gallart, J., and Nicolich, R. (2000). Mount Etna dense array local earthquake P and S tomography and implications for volcanic plumbing. J. Geophys. Res. Solid Earth *105*, 21633–21646.

Legrand, D., Kaneshima, S., and Kawakatsu, H. (2000). Moment tensor analysis of near-field broadband waveforms observed at Aso Volcano, Japan. J. Volcanol. Geotherm. Res. *101*, 155–169.

Lokmer, I., and Bean, C.J. (2010). Properties of the near-field term and its effect on polarisation analysis and source locations of long-period (LP) and very-long-period (VLP) seismic events at volcanoes. J. Volcanol. Geotherm. Res. *192*, 35–47.

Lokmer, I., Bean, C.J., Saccorotti, G., and Patanè, D. (2007). Moment-tensor inversion of LP events recorded on Etna in 2004 using constraints obtained from wave simulation tests. Geophys. Res. Lett. *34*.

Lokmer, I., Saccorotti, G., Di Lieto, B., and Bean, C.J. (2008). Temporal evolution of long-period seismicity at Etna Volcano, Italy, and its relationships with the 2004–2005 eruption. Earth Planet. Sci. Lett. *266*, 205–220.

Luca, G.D., Filippi, L., Patanè, G., Scarpa, R., and Vinciguerra, S. (1997). Three-dimensional velocity structure and seismicity of Mt. Etna Volcano, Italy. J. Volcanol. Geotherm. Res. *79*, 123–138.

Maday, Y., and Patera, A.T. (1989). Spectral element methods for the incompressible Navier-Stokes equations. In State-of-the-Art Surveys on Computational Mechanics (A90-47176 21-64). New York, American Society of Mechanical Engineers, 1989, P. 71-143. Research Supported by DARPA., pp. 71–143.

Maeda, Y., Takeo, M., and Ohminato, T. (2011). A waveform inversion including tilt: method and simple tests: A waveform inversion including tilt. Geophys. J. Int. *184*, 907–918.

Maufroy, E., Chaljub, E., Hollender, F., Kristek, J., Moczo, P., Klin, P., Priolo, E., Iwaki, A., Iwata, T., Etienne, V., et al. (2015). Earthquake Ground Motion in the Mygdonian Basin, Greece: The E2VP Verification and Validation of 3D Numerical Simulation up to 4 Hz. Bull. Seismol. Soc. Am.

Menke, W. (1989). Geophysical Data Analysis: Discrete Inverse Theory (Boston: Academic Press).

Moczo, P., Kristek, J., and Gális, M. (2014). The Finite-Difference Modelling of Earthquake Motions: Waves and Ruptures (Cambridge University Press).

Nakano, M., and Kumagai, H. (2005). Waveform inversion of volcano-seismic signals assuming possible source geometries. Geophys. Res. Lett. *32*, n/a – n/a.

Nakano, M., Kumagai, H., and Chouet, B.A. (2003). Source mechanism of long-period events at Kusatsu–Shirane Volcano, Japan, inferred from waveform inversion of the effective excitation functions. J. Volcanol. Geotherm. Res. *122*, 149–164.

Neuberg, J., and Pointer, T. (2000). Effects of volcano topography on seismic broad-band waveforms. Geophys. J. Int. *143*, 239–248.

Ohminato, T., Chouet, B.A., Dawson, P., and Kedar, S. (1998). Waveform inversion of very long period impulsive signals associated with magmatic injection beneath Kilauea volcano, Hawaii. J. Geophys. Res. Solid Earth *103*, 23839–23862.

Pasquare, G., Servizio geologico., Italy., Consiglio Nazionale delle Ricerche., and Commissione per la Cartopgrafia Geologica e Geomorfologica. (1992). Carta geologica d'Italia, 1: 50.000 : guida al rilevamento (Rome: Servizio Geologico Nazionale).

Patane, D., Chiarabba, C., Cocina, O., De Gori, P., Moretti, M., and Boschi, E. (2002). Tomographic images and 3D earthquake locations of the seismic swarm preceding the 2001 Mt. Etna eruption: Evidence for a dyke intrusion. Geophys. Res. Lett. *29*, 135–1 – 135–4.

Patanè, D., Aliotta, M., Cannata, A., Cassisi, C., Coltelli, M., Di Grazia, G., Placido, M., and Zuccarello, L. (2011). Interplay between Tectonics and Mount Etna's Volcanism: Insights into the Geometry of the Plumbing System. New Front. Tecton. Res. - Midst Plate Converg. Dr Uri Schattner Ed.

Patera, A.T. (1984). A spectral element method for fluid dynamics : laminar flow in a channel expansion (J. Comput. Phys. 54, 468–488.).

Potter, C.C., and Stewart R.R. (1998). Density predictions using Vp and Vs sonic logs. CREWES Res. Rep. *10*.

Romano, R., Lentini, F., and Sturiale, C. (1979). Carta geologica del Monte Etna, scala 1:50.000 (Mem. Soc. Geo. Italiana).

Saccorotti, G., Zuccarello, L., Del Pezzo, E., Ibanez, J., and Gresta, S. (2004). Quantitative analysis of the tremor wavefield at Etna Volcano, Italy. J. Volcanol. Geotherm. Res. *136*, 223–245.

Saccorotti, G., Lokmer, I., Bean, C.J., Di Grazia, G., and Patanè, D. (2007). Analysis of sustained long-period activity at Etna Volcano, Italy. J. Volcanol. Geotherm. Res. *160*, 340–354.

Seriani, G., and Oliveira, S.P. (2008). Dispersion analysis of spectral element methods for elastic wave propagation. Wave Motion *45*, 729–744.

Thomson, W.T. (1950). Transmission of Elastic Waves through a Stratified Solid Medium. J. Appl. Phys. *21*, 89–93.

Thun, J., Lokmer, I., and Bean, C.J. (2015). New observations of displacement steps associated with volcano seismic long-period events, constrained by step table experiments. Geophys. Res. Lett. *42*, 3855–3862.

Vasco, D.W. (1989). Deriving source-time functions using principal component analysis. Bull. Seismol. Soc. Am. *79*, 711–730.

Vavryčuk, V. (2001). Inversion for parameters of tensile earthquakes. J. Geophys. Res. Solid Earth *106*, 16339–16355.

Villaseñor, A., Benz, H.M., Filippi, L., De Luca, G., Scarpa, R., Patanè, G., and Vinciguerra, S. (1998). Three-dimensional P-wave velocity structure of Mt. Etna, Italy. Geophys. Res. Lett. *25*, 1975–1978.

Waltershausen, W.S. (1844). Atlas des Aetna (Berlin: Gottingen, Weimar).

Waltershausen, W.S. (1880). Der Aetna (Engelman, Leipzig).

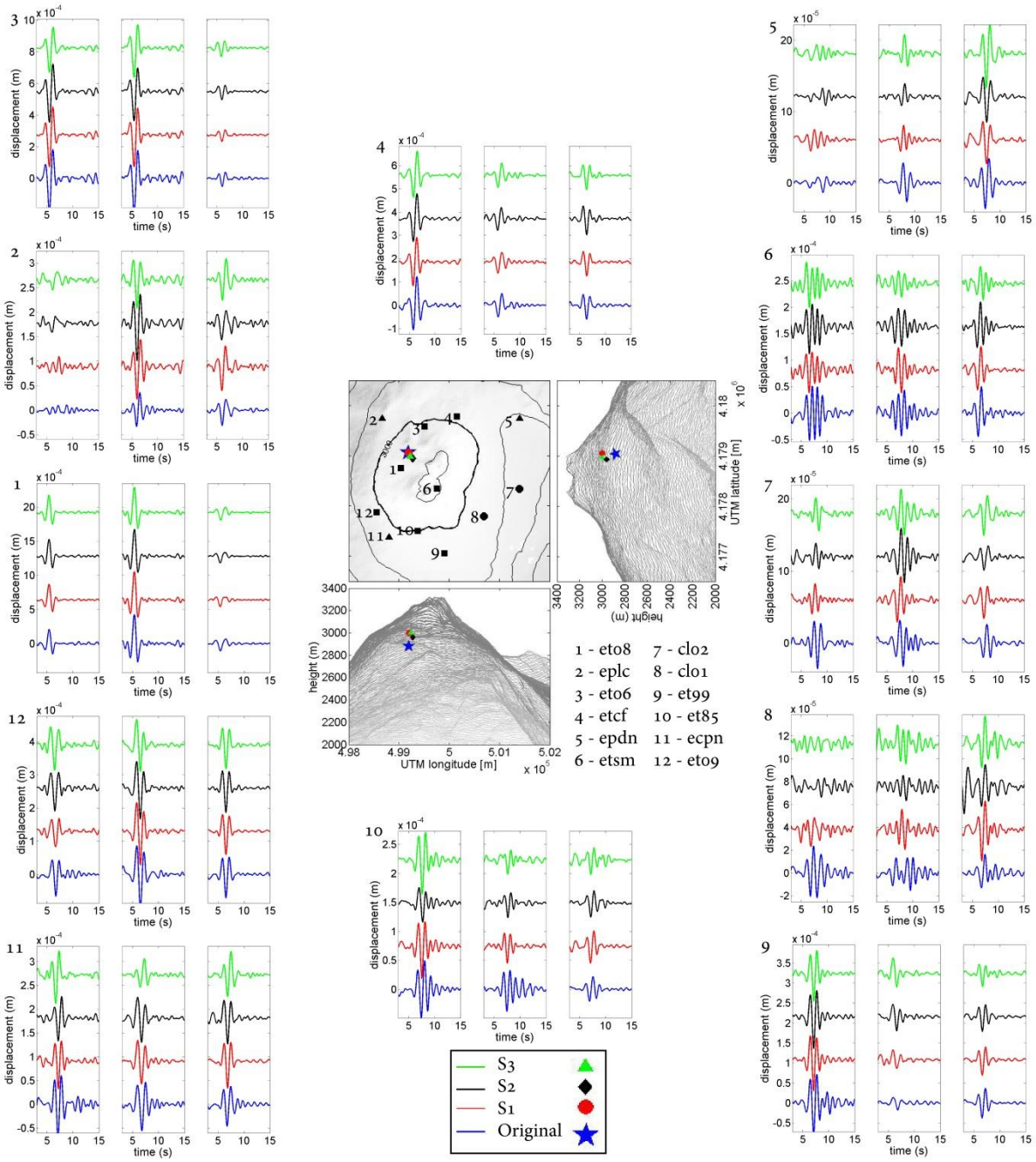

Appendix A

Waveform comparison between the synthetic (velocity model *S4*) and retrieved signals after the inversion using velocity models *S1*, *S2*, and *S3* for the shallow source. Three components of displacement for each station (x, y, z) are represented. The central map represents the stations used in the inversion. Numbers nearby each stations name are related to the corresponding box where waveforms are compared. The true and the retrieved hypocenter positions are plotted in the center panel.

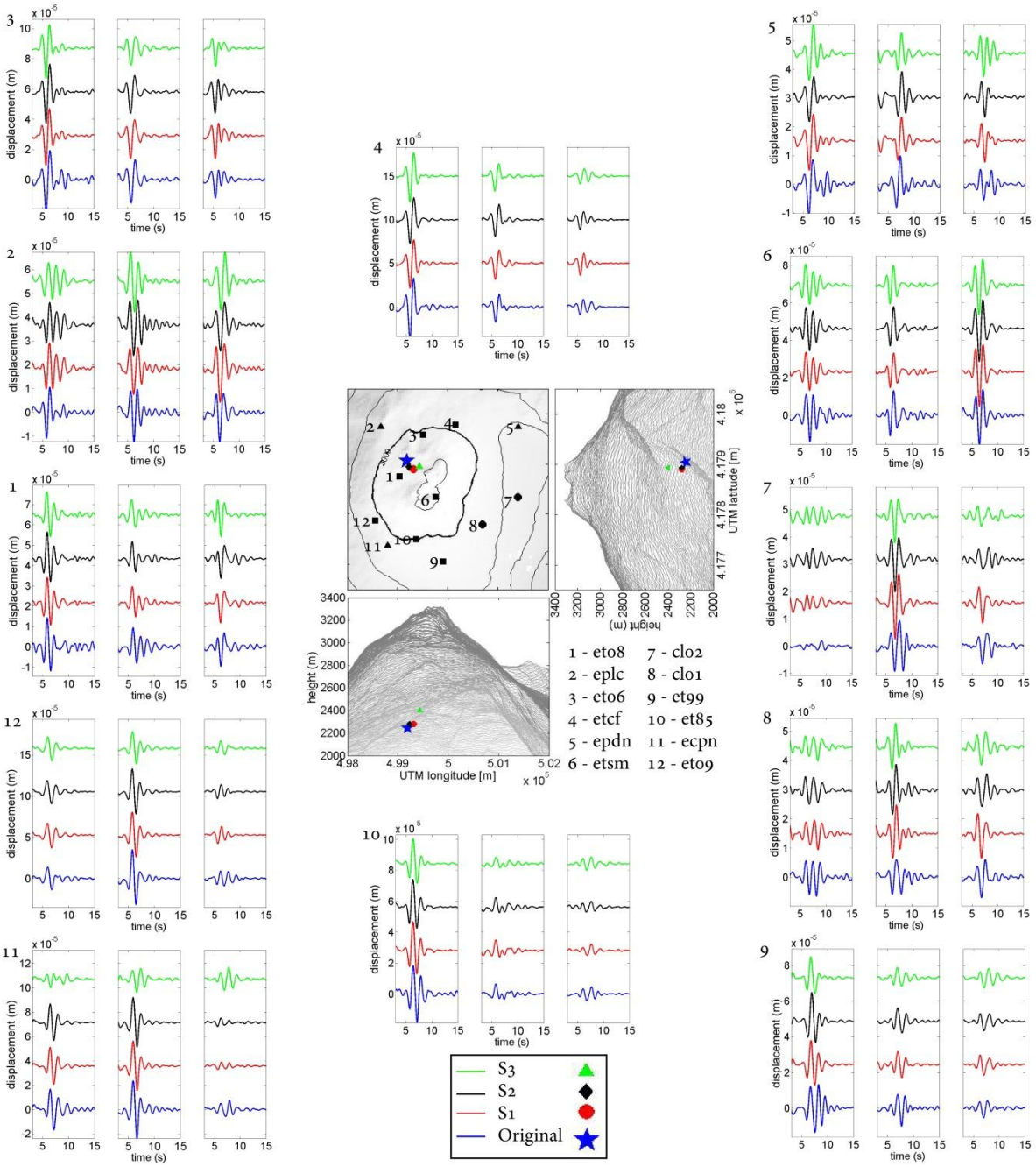

Appendix B

Waveforms comparison between the synthetic (velocity model *S4*) and retrieved signals after the inversion using Green's functions from velocity models *S1*, *S2*, and *S3* for the deep source. See also Appendix A.

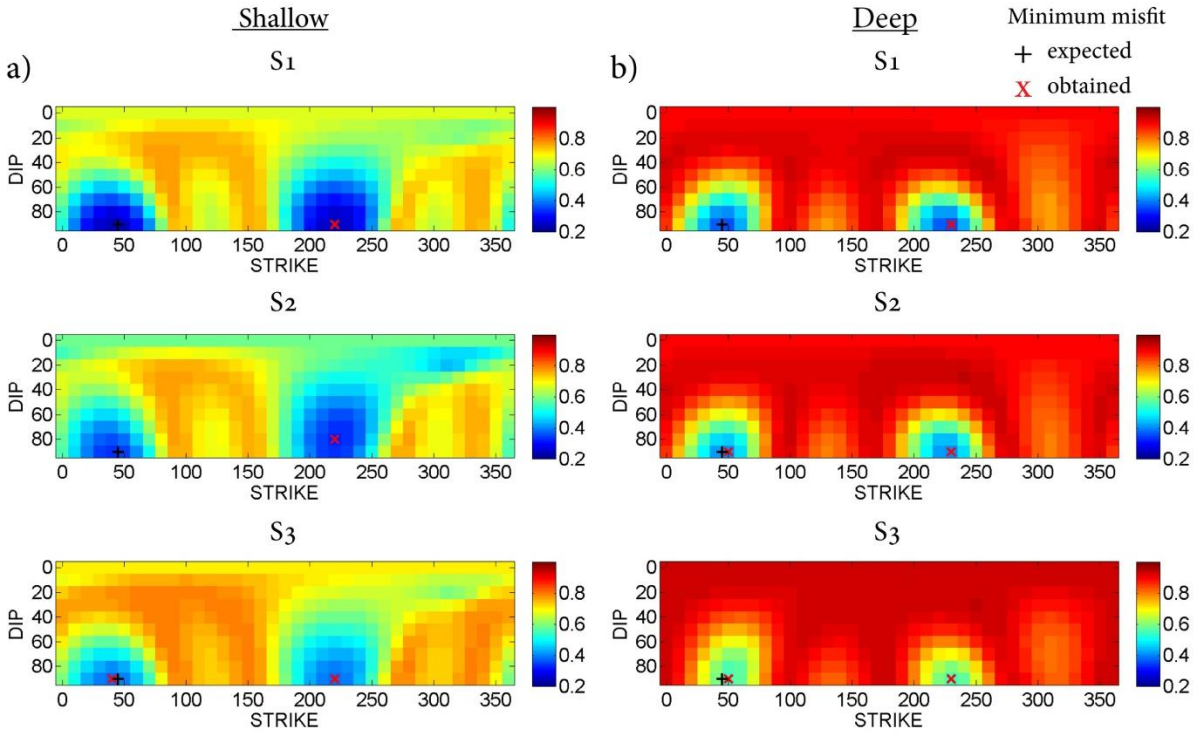

Appendix C

Misfit in parameter search (strike φ, dip θ) under MT+F inversion supposing a tensile crack. The minimum retrieved misfit is represented by a [*x*] and the given value by [+].

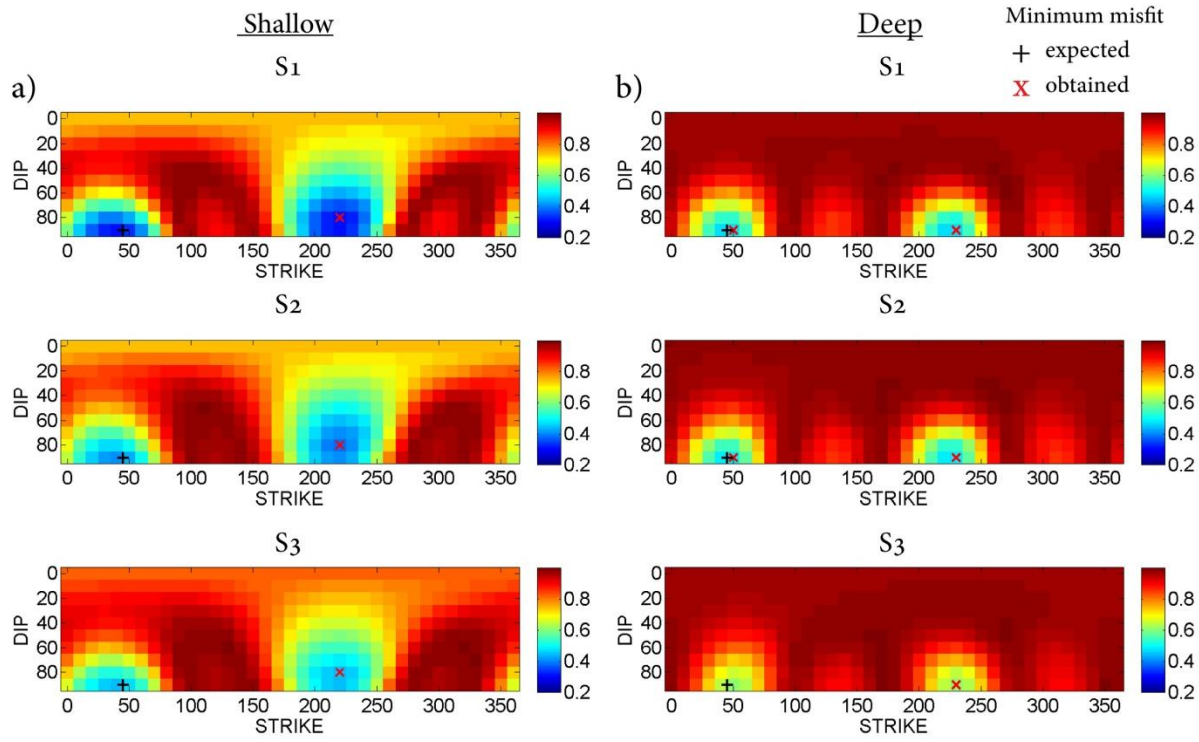

Appendix D

Misfit in parameter search (strike φ, dip θ) under MT inversion supposing a tensile crack. The minimum retrieved misfit is represented by a [*x*] and the given value by [+].

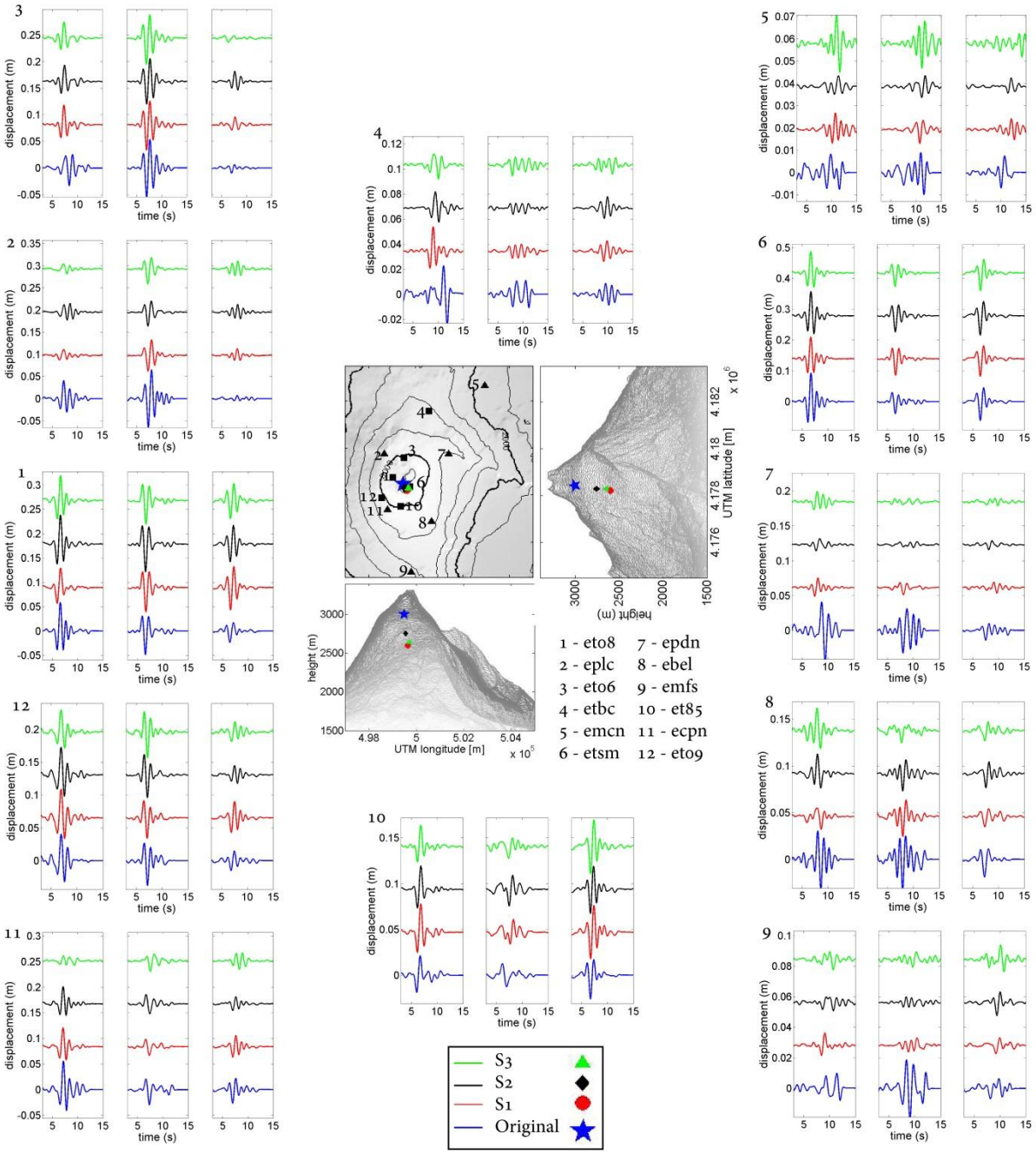

Appendix E

Waveforms comparison between the filtered (0.1 – 1.2 Hz) observed signals and the synthetics filtered. The used receiver position and the obtained hypocenter location from each inversion for the LP event recorded on Mt. Etna (2008) are shown. A star represents the solution obtained by De Barros et al. (2009).

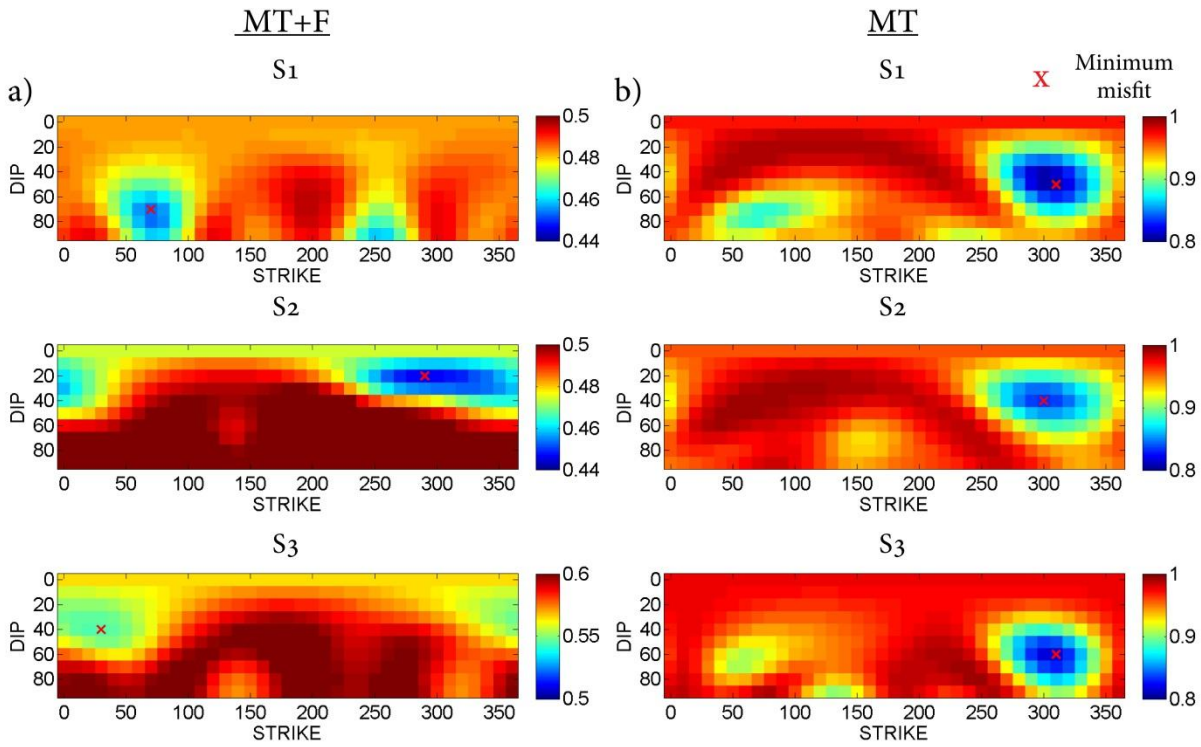

Appendix F

Misfit plot of the crack orientation (strike φ and dip θ) supposing a tensile crack in constrained MT+F and MT inversion for each structure model.

Table 1 Summary of the results in MT+F and MT inversions for the shallow vertical crack, using different structure models (S1, S2 and S3), respectively. For the best misfit in each inversion, the fault mechanism (strike, dip) are calculated and the decompositions are performed. We also report the validation misfit between the observed MT solution and the original one used to reproduce the tensile crack in the synthetic test. M_w represents the moment magnitude of the seismic event. For comparison, true model parameters are reported at the bottom.

Inversion	*Structural model*	*Misfit*	*Validation Misfit*	ϕ	θ	*ISO (%)*	*CLVD (%)*	*DC(%)*	M_w
	S1	0.123	28.97	53.5	17.4	54	40	6	2.5
MT+F	*S2*	0.155	2.20	47.1	17.4	52	35	12	2.1
	S3	0.219	3.43	48.5	19.1	55	39	6	2.2
	S1	0.174	4.63	44.9	27.7	55	2	43	2.1
MT	*S2*	0.240	0.87	41.3	65.4	45	15	40	1.7
	S3	0.291	0.85	42.0	60.7	45	6	48	1.7
True Parameters	***S4***	**-**		***45***	***90***	***55***	***45***	***0***	***2***

Table 2 Summary of the results in MT+F and MT inversions for the deep vertical crack. See also the caption of Table 1.

Inversion	*Structural model*	*Misfit*	*Validation Misfit*	ϕ	θ	*ISO (%)*	*CLVD (%)*	*DC(%)*	M_w
	S1	0.250	0.74	45.4	91.7	47	48	6	1.7
MT+F	*S2*	0.269	0.82	46.4	90.9	48	46	6	1.6
	S3	0.412	0.93	51.8	79.0	53	31	16	1.6
	S1	0.341	0.54	43.3	88.0	57	26	17	1.7
MT	*S2*	0.344	0.67	45.1	87.9	58	26	16	1.6
	S3	0.490	0.72	50.3	83.2	55	34	11	1.6
True Parameters	***S4***	**-**		***45***	***90***	***55***	***45***	***0***	***2***

Table 3 Obtained minimum misfit values in constrained inversion (crack and explosion) and crack orientation (φ,θ). Note that the given crack mechanism is a tensile with φ=45° and θ=90°. Parameter searches are performed every 10°.

	Oriented Crack					
	MT+F			**MT**		
	Shallow					
Structural model	*Misfit*	ϕ	θ	*Misfit*	ϕ	θ
S1	0.324	40	90	0.303	40	90
S2	0.327	40	90	0.385	40	80
S3	0.384	40	90	0.443	40	80
	Deep					
S1	0.358	50	90	0.470	50	90
S2	0.404	50	90	0.485	50	90
S3	0.550	50	90	0.608	50	90
	Explosion					
	Shallow					
S1	0.3852	-	-	0.5655	-	-
S2	0.4275	-	-	0.6297	-	-
S3	0.5162	-	-	0.6692	-	-
	Deep					
S1	0.8395	-	-	0.9422	-	-
S2	0.8388	-	-	0.9333	-	-
S3	0.8654	-	-	0.9517	-	-

Table 4 Inversion results for a LP event recorded on Etna in different inversion settings. For comparison, the result of De Barros et al. (2011) is also shown at the bottom. MT-only inversion results for model S2 are missing as the retrieved STFfor different MT components were not represented by a unique source-time history (more than one significant singular values present in the SVD decomposition of the solution). This is normally due to inability of the MT-only solution to account for the uncertainties in the velocity model (it can be often observed when performing MT inversion of real data).

.

Inversion	*Structural model*	*Misfit*	ϕ	θ	*ISO (%)*	*CLVD (%)*	*DC(%)*
	S1	0.386	85.8	82.4	92	2	6
MT+F	*S2*	0.349	90.0	21.4	79	14	7
	S3	0.453	48.1	67.2	90	3	7
	S1	0.637	78.9	12.7	82	1	17
MT	*S2*	0.703	-	-	-	-	-
	S3	0.684	27.0	71.5	78	12	10
De Barros (2011)		-	340	50	80	-	-

Table 5 Constrained inversion results (misfit and mechanism) for a tensile crack and an explosion for the 2008 LP event occurred on Etna.

	Crack					
	MT+F			**MT**		
Structural model	*Misfit*	ϕ	θ	*Misfit*	ϕ	θ
S1	0.454	70	70	0.806	310	50
S2	0.446	290	20	0.833	300	40
S3	0.544	30	40	0.817	310	60
	Explosion					
S1	0.443	-	-	0.953	-	-
S2	0.425	-	-	0.629	-	-
S3	0.545	-	-	0.975	-	-

1)

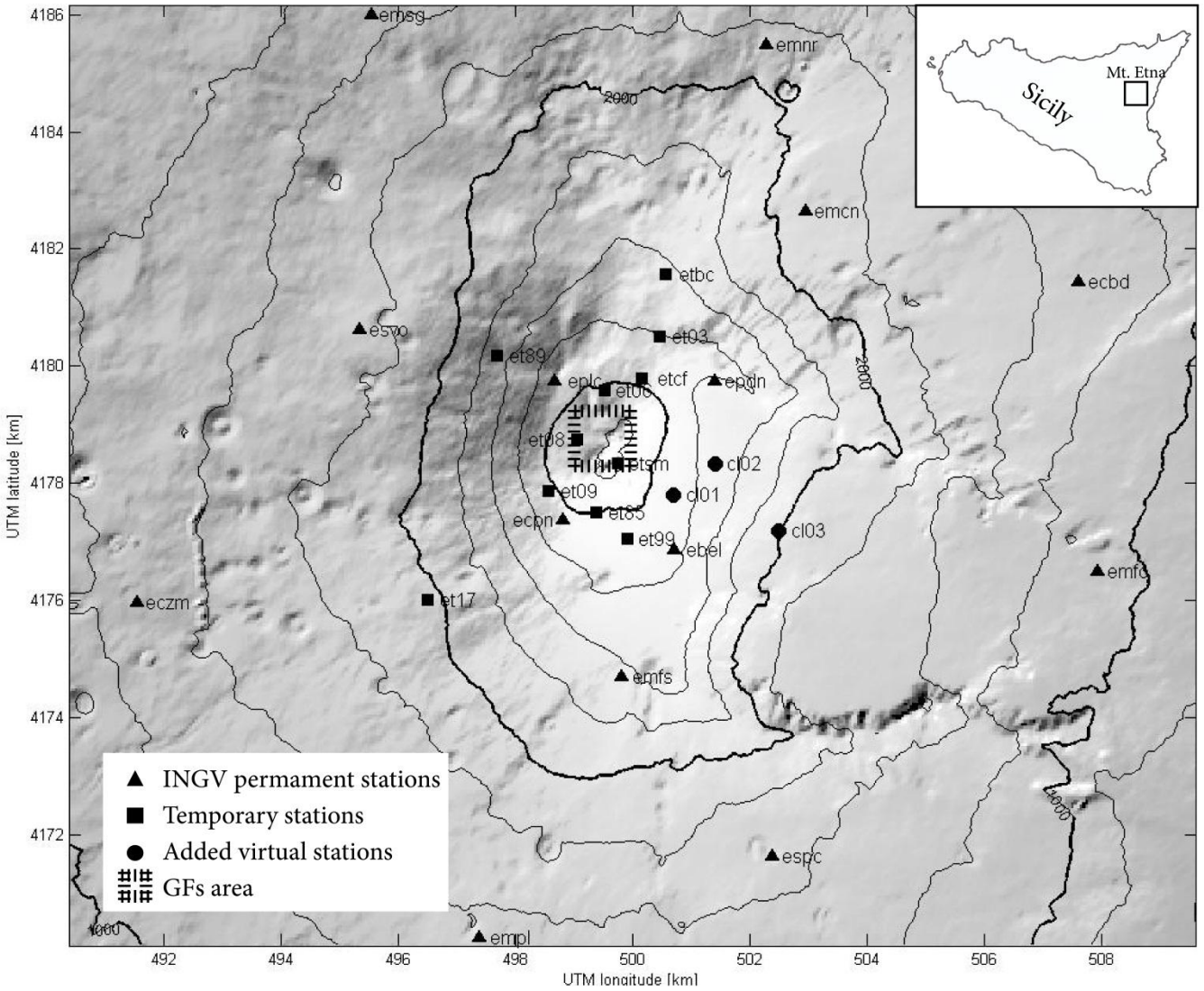

Figure 1. Map of Mount Etna and receivers locations used in this study, the straight hash line indicates the source area for which the Green functions are calculated.

2)

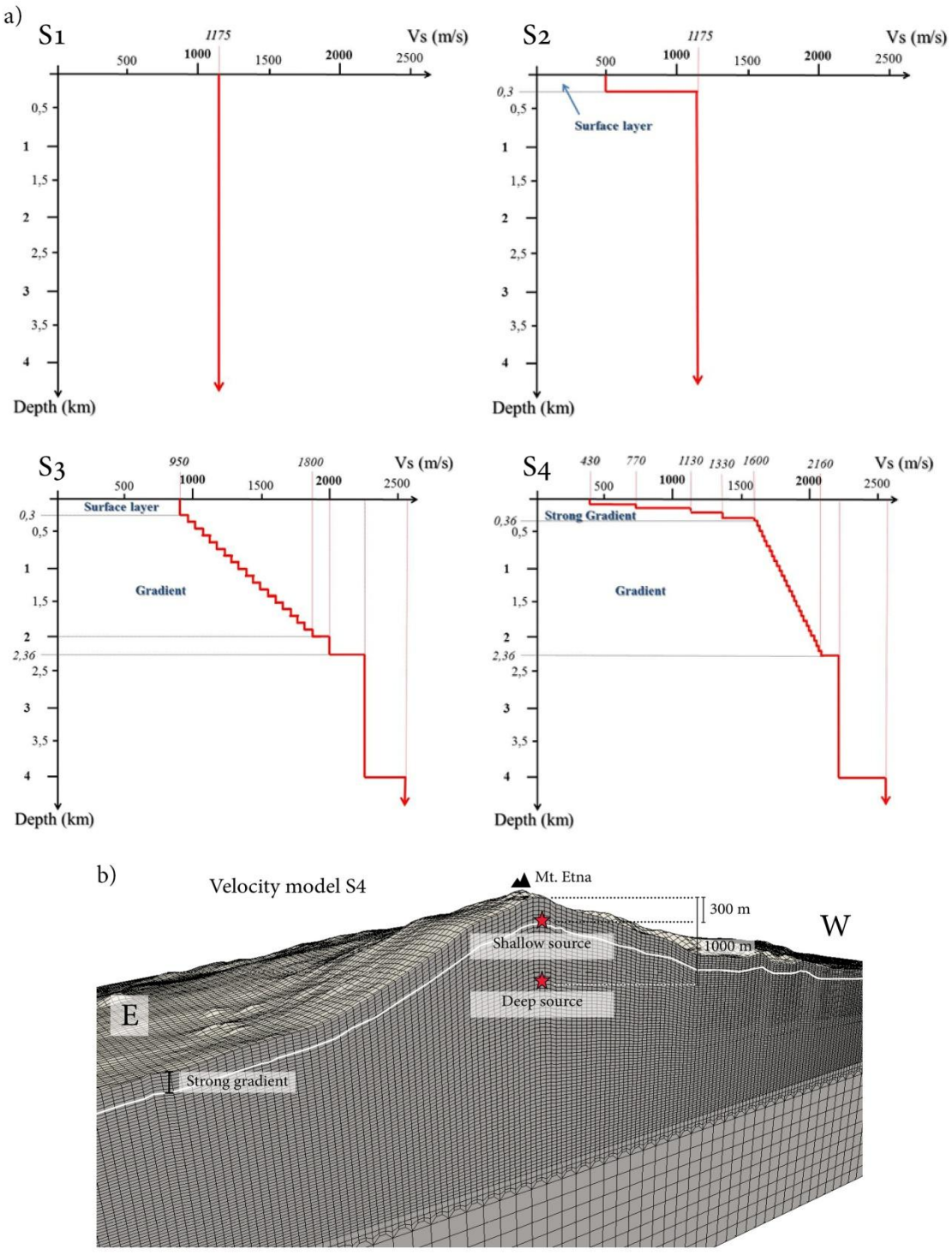

Figure 2. a) *Vs* velocity profiles of the four considered models. *S1*, *S2* and *S3* are the models used for the inversion while *S4* is the model used to prepare the synthetics. b) Example of E-W cross section of model *S4* in correspondence of the summit of Mt. Etna volcano. Thin black lines represent the discretization of the velocity model in hexahedral elements and white line represents the limit of the shallow low velocity zone characterized by a strong velocity gradient. We also report the location of shallow and deep sources for comparison.

3)

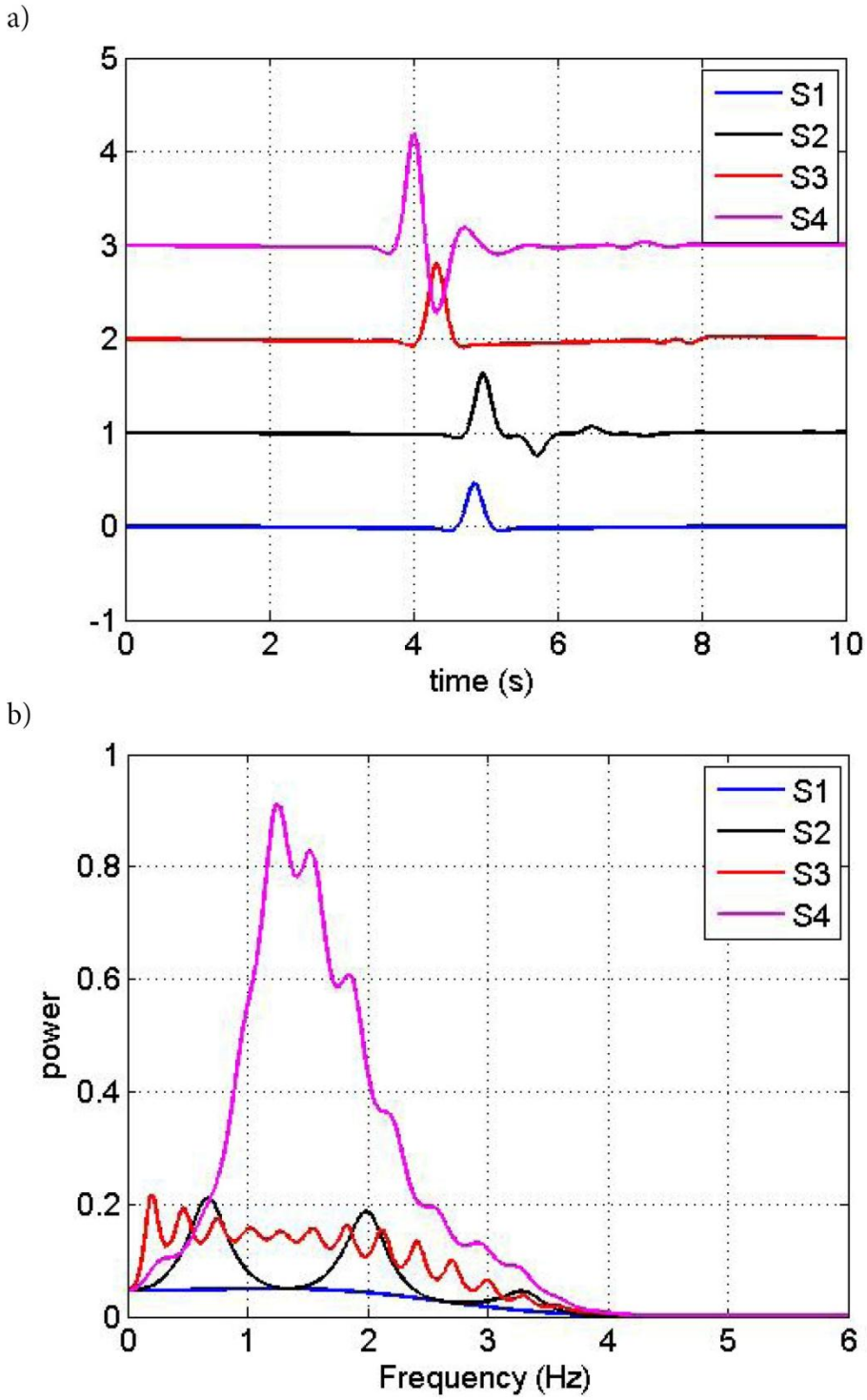

Figure 3. a) Recorded filtered (0.2 – 2 Hz) velocity traces at the surface for an impulse point source generating a plane wave (SH) embedded at 3 km depth. Wave propagation is computed for four different velocity models (S1, S2, S3 and S4) constituted of plane stacked layer with geological properties and thickness

corresponding to the velocity models represented in Fig. 2. b) Frequency content of the recorded velocity traces of Fig. 3a.

4)

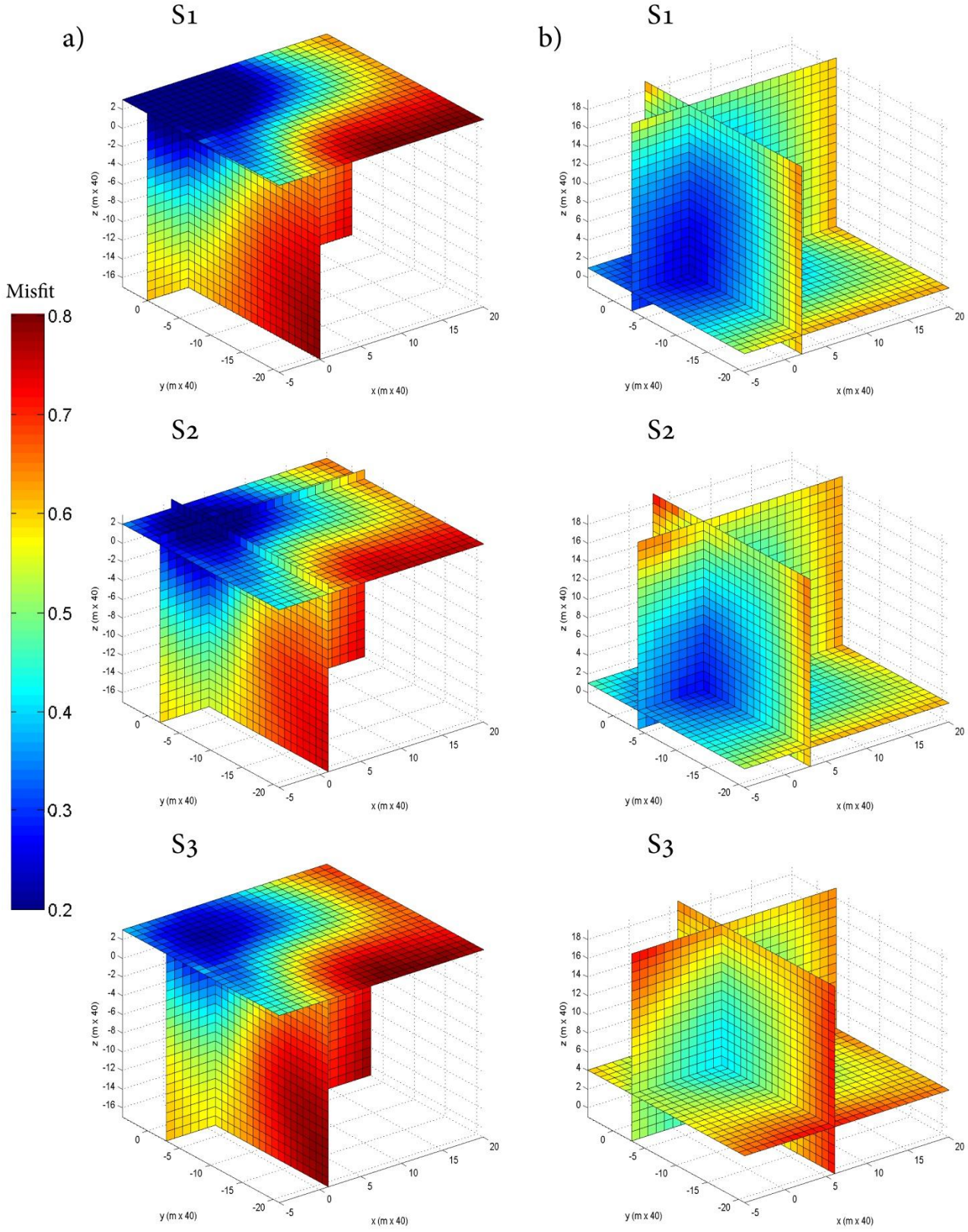

Figure 4. Source location for shallow (left) and deep (right) source obtained in the inversion of minimum R using different structure models. Axes represent the relative source location with a 40 m spacing. The real source position is represented by (0,0,0). From top to bottom velocity models *S1*, *S2*, and *S3* used for the inversion. Lowest misfit value is represented by the synthetic slices intersection for each velocity model.

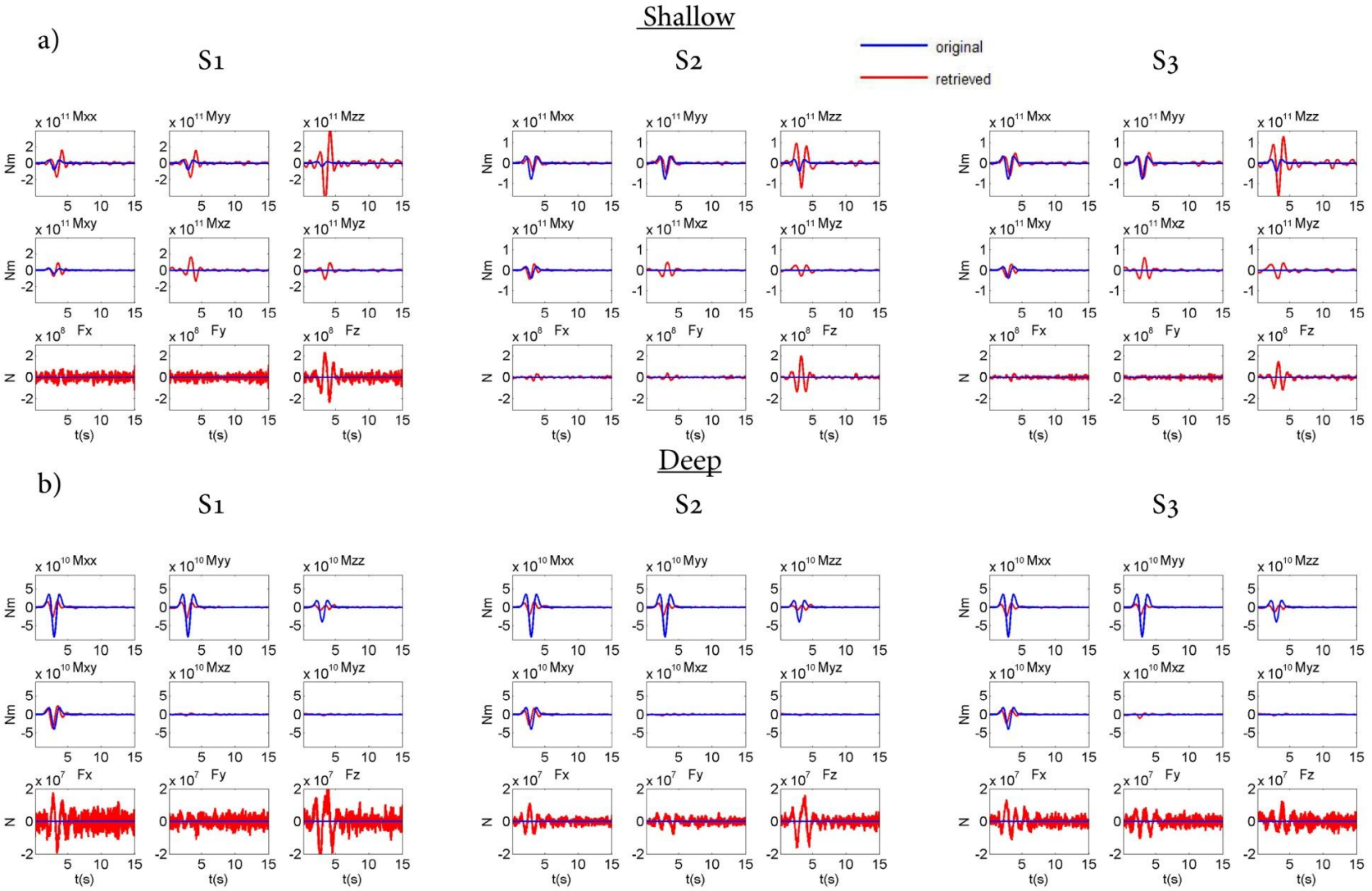

5)

Figure 5. Comparison between original (blue) and retrieved (red) source time functions for the MT+F (including forces) inversion for three velocity models and for both source depths. Six moment tensor components and three single forces are represented.

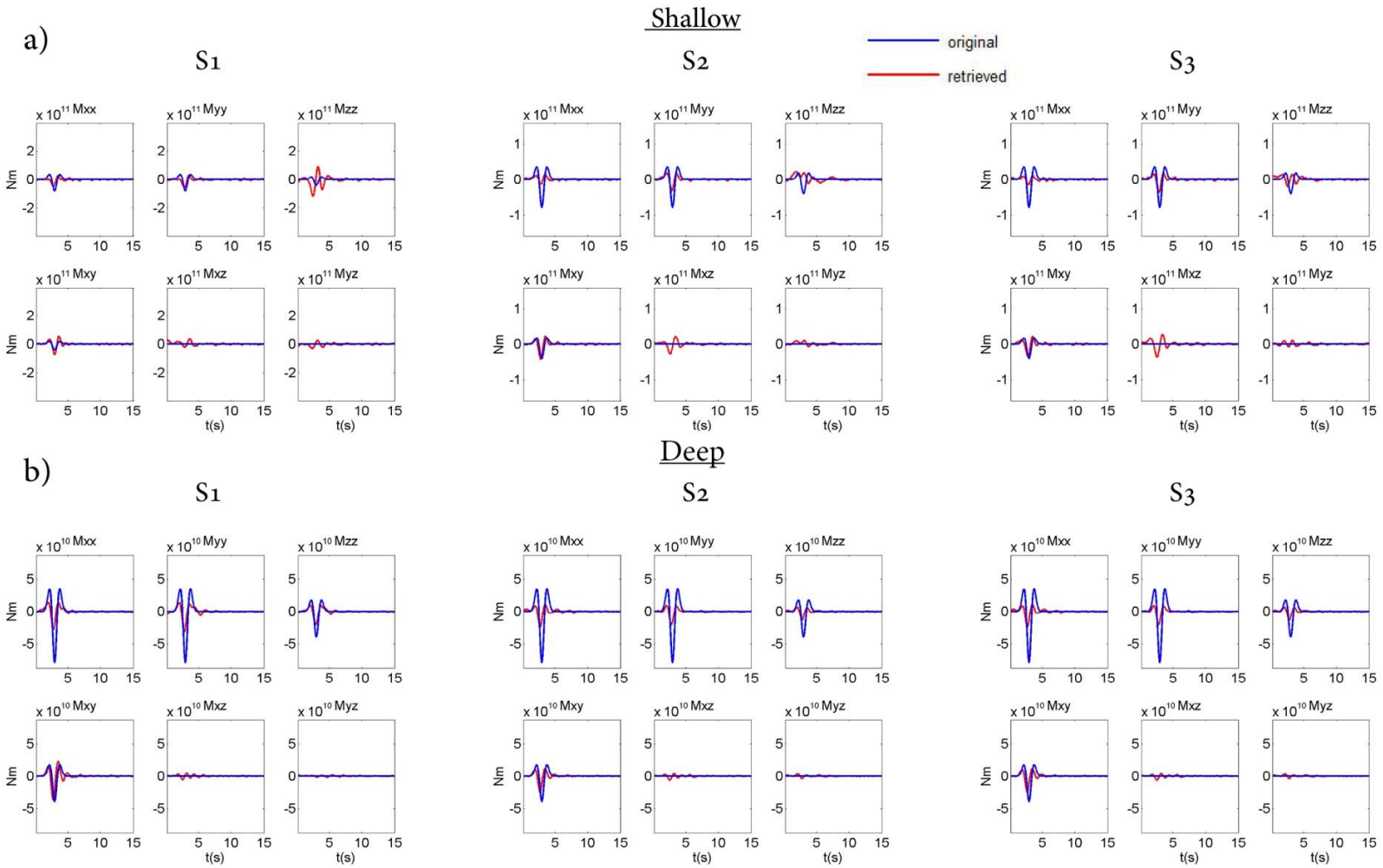

6)

Figure 6. Comparison between original (blue) and retrieved (red) source time functions for the MT inversion for three velocity models and for both source depths. Six moment tensor components are represented for each model.

7)

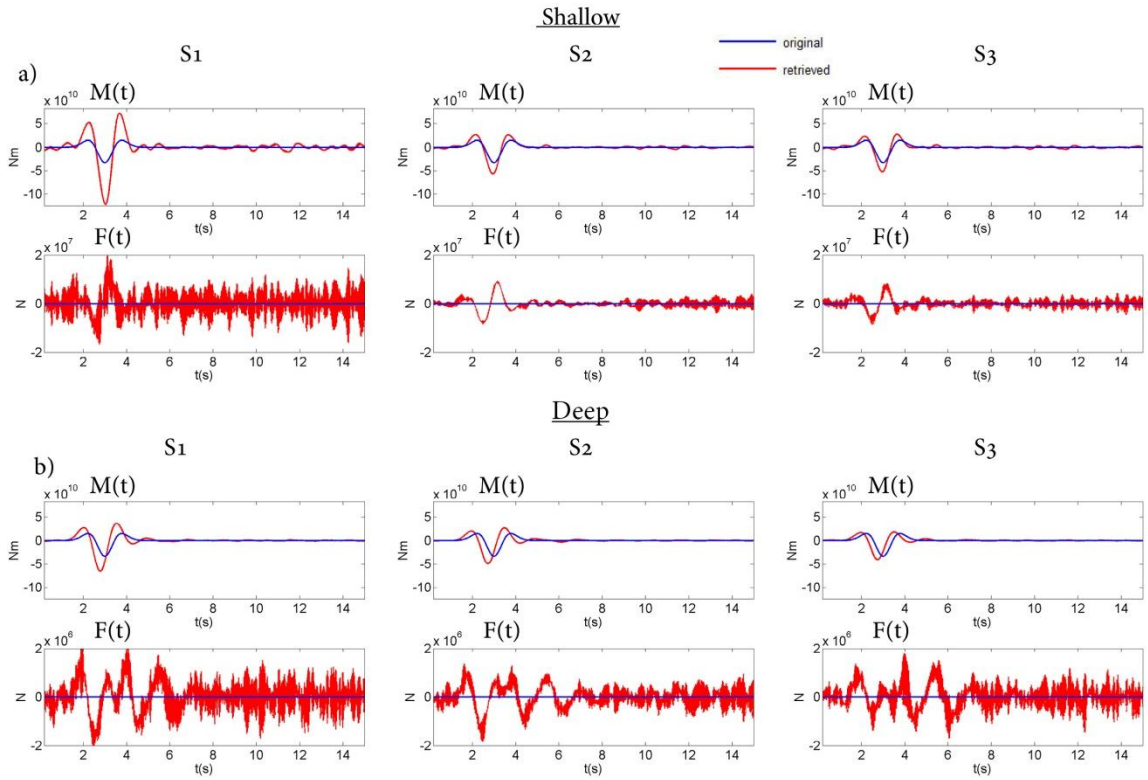

Figure 7. Comparison between original and best retrieved source time function in the constrained MT+F inversion for a tensile crack. For comparison the vertical and most energetic single force (F_z) is plotted. (a) Shallow source, (b) Deep source. Three structure models are used.

8)

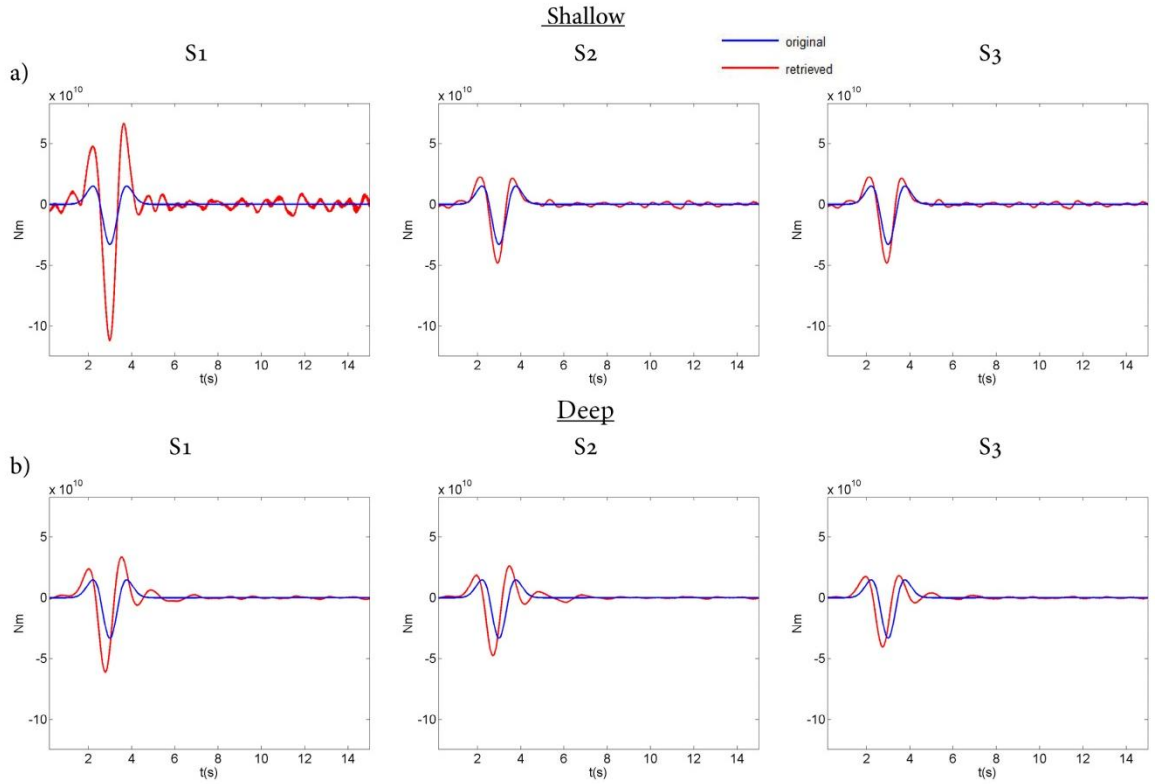

Figure 8. Comparison between original and best retrieved source time function in the constrained MT inversion for a tensile crack. (a) Shallow source, (b) Deep source. Three structure models are used.

9)

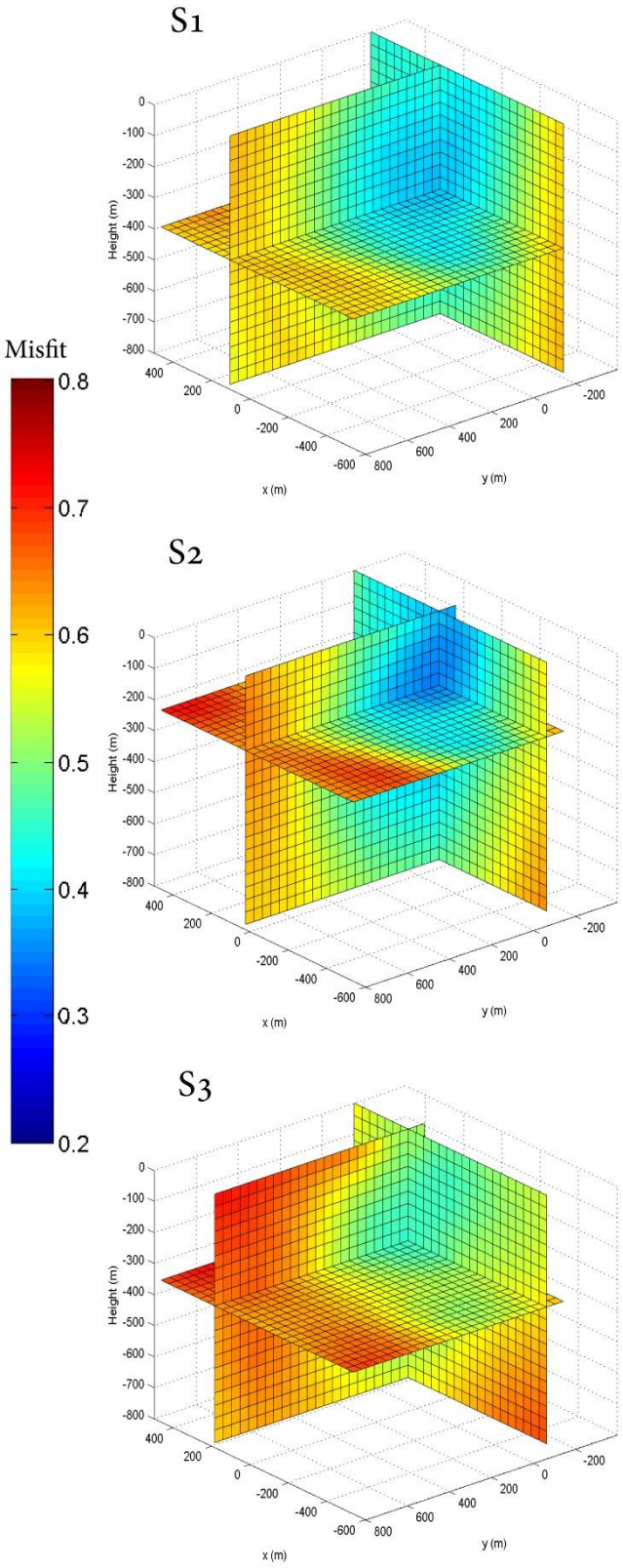

Figure 9. Misfit with respect to the source position for the LP event. The location through MT inversion is conducted in three different velocity models (*S1*, *S2* and *S3* respectively). The axes in meters represent the relative distance to the original source location determined by De Barros et al. (2011). Original solution (x, longitude, 49950 Km, y, latitude, 4178450 Km, z, height, 3 Km).

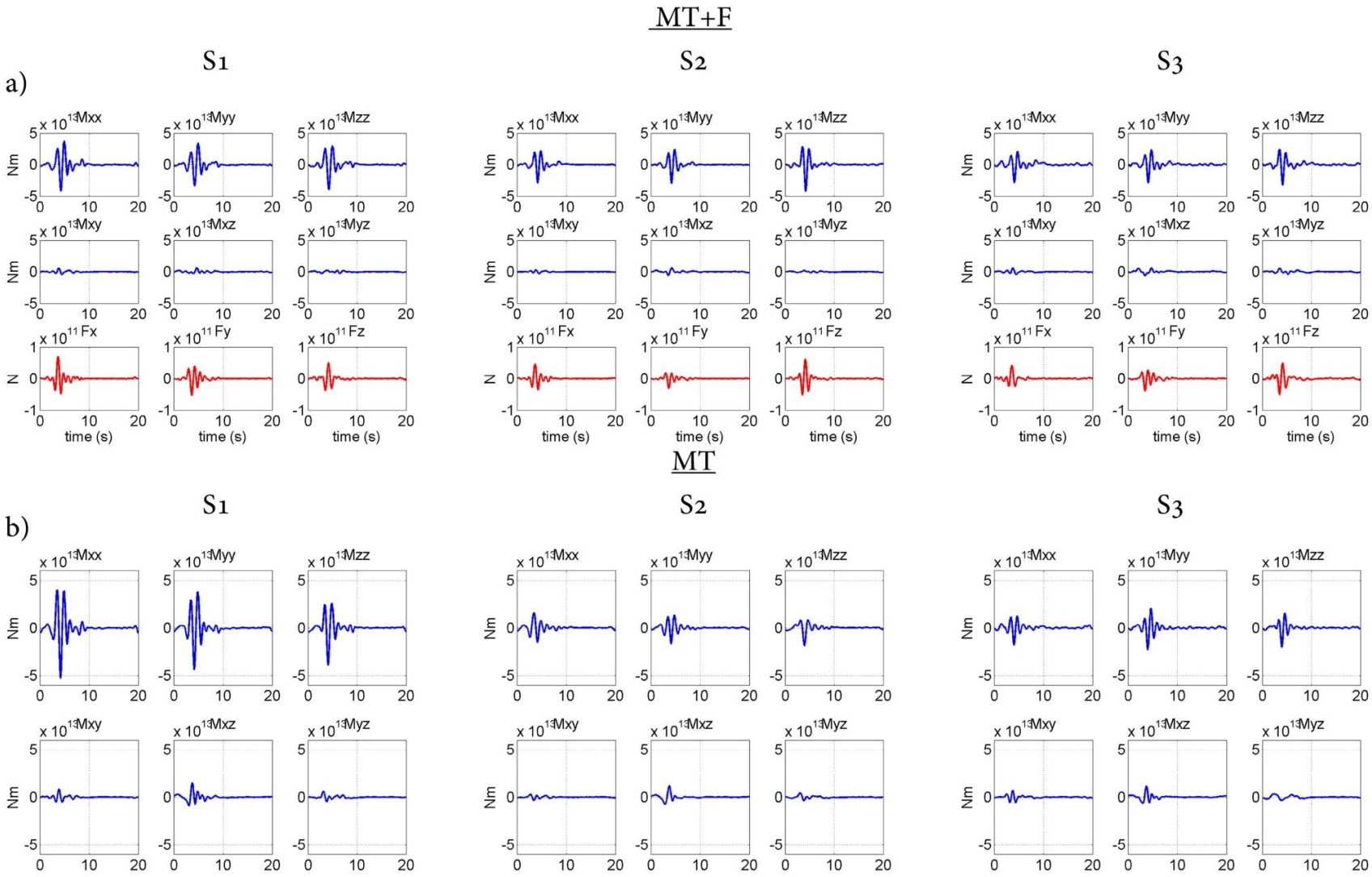

10)

Figure 10. Comparison of source time functions for each MT and MT+F inversion in each of the three velocity models.

11)

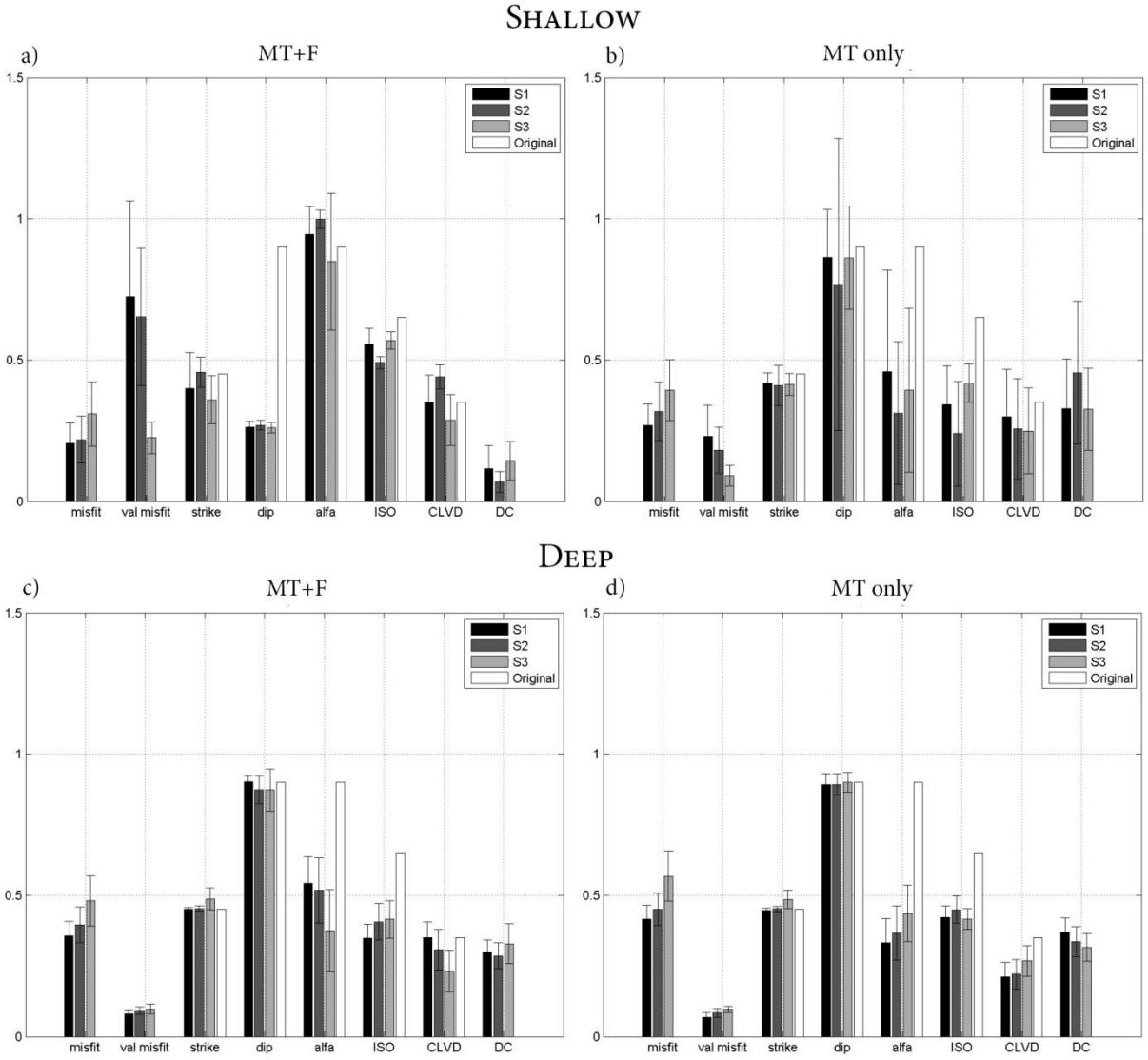

Figure 11. Median and median absolute deviations for misfit, validation misfit and MT decomposition solutions obtained for 1350 MT inversions performed varying the number and the position of the seismic stations. The results are shown for all the three velocity models. White bars correspond to the expected result for each parameter. Some parameters are scaled for readability: validation misfit, strike, dip and alfa are scaled by a factor of 10; ISO, CLVD

and DC are scaled by a factor of 100. Shallow source a) MT+F solution, b) MT-only solution; Deep source c) MT+F solution, b) MT-only solution.

12)

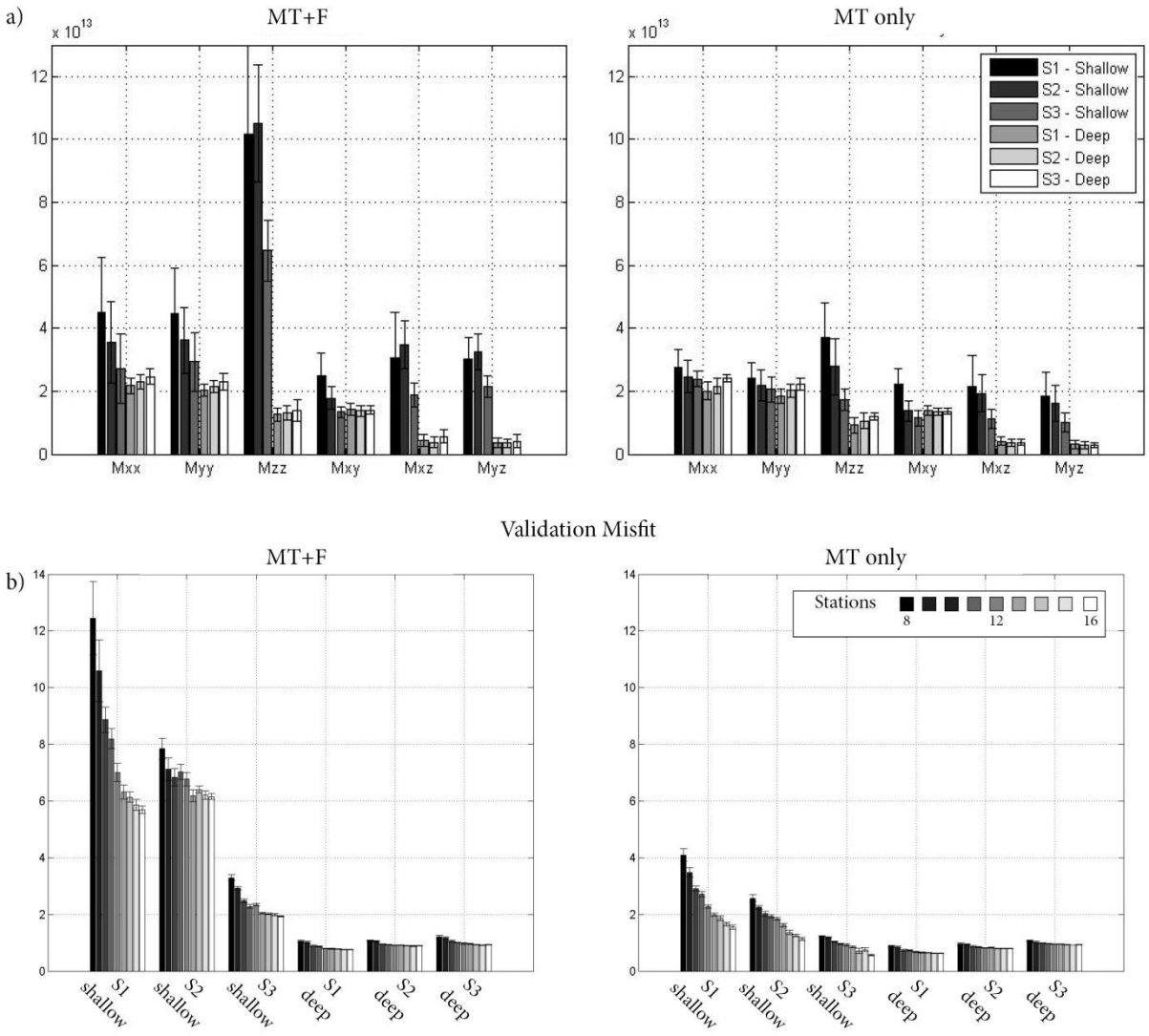

Figure 12. a) Validation misfits (calculated with L1-norm) for each MT component computed independently. Validation misfits and errors are computed as in Fig. 11. MT+F solution (left) and MT-only solution (right) for both sources and the three velocity models. b) MT solution of the overall validation misfit and its variation varying the number of seismic stations for each source and velocity model. The bars corresponds to the solutions including from 8 to 16 stations of the seismic network (Fig. 1) excluding stations located nearby the borders of the synthetic domain. Results are computed as in Fig. 11, but for 150 MT inversions each. MT+F solution (left) and MT-only solution (right) for both sources and the three velocity models.